



Fort, Loic and Batista, José Miguel and Thomason, Peter A. and Spence, Heather J. and Whitelaw, Jamie A. and Tweedy, Luke and Greaves, Jennifer and Martin, Kirsty J. and Anderson, Kurt I. and Brown, Peter and Lilla, Sergio and Neilson, Matthew P. and Tafelmeyer, Petra and Zanivan, Sara and Ismail, Shehab and Bryant, David M. and Tomkinson, Nicholas C. O. and Chamberlain, Luke H. and Mastick, Grant S. and Insall, Robert H. and Machesky, Laura M. (2018) Fam49/CYRI interacts with Rac1 and locally suppresses protrusions. Nature Cell Biology, 20. pp. 1159-1171. , <http://dx.doi.org/10.1038/s41556-018-0198-9>

This version is available at <https://strathprints.strath.ac.uk/65553/>

Strathprints is designed to allow users to access the research output of the University of Strathclyde. Unless otherwise explicitly stated on the manuscript, Copyright © and Moral Rights for the papers on this site are retained by the individual authors and/or other copyright owners. Please check the manuscript for details of any other licences that may have been applied. You may not engage in further distribution of the material for any profitmaking activities or any commercial gain. You may freely distribute both the url (<https://strathprints.strath.ac.uk/>) and the content of this paper for research or private study, educational, or not-for-profit purposes without prior permission or charge.

Any correspondence concerning this service should be sent to the Strathprints administrator: strathprints@strath.ac.uk

1
2 Fam49/CYRI interacts with Rac1 and locally suppresses protrusions

3
4
5 Loic Fort^{1,2*}, José Miguel Batista^{1,2*}, Peter A. Thomason¹, Heather J. Spence¹, Jamie
6 A. Whitelaw¹, Luke Tweedy¹, Jennifer Geaves³, Kirsty J. Martin¹, Kurt I.
7 Anderson^{1,4}, Peter Brown¹, Sergio Lilla¹, Matthew P. Neilson¹, Petra Tafelmeyer⁵,
8 Sara Zanivan¹, Shehab Ismail^{1,2}, David M. Bryant^{1,2}, Nicholas C.O. Tomkinson⁶,
9 Luke H. Chamberlain³, Grant S. Mastick⁷, Robert H. Insall^{‡1,2} and Laura M.
10 Machesky^{‡1,2}

11
12 Affiliations:

- 13 1. CRUK Beatson Institute, Switchback Road, Glasgow G61 1BD, UK
- 14 2. University of Glasgow Institute of Cancer Sciences, Switchback Road, Glasgow
15 G61 1BD, UK
- 16 3. Strathclyde Institute of Pharmacy and Biomedical Sciences, University of
17 Strathclyde, 161 Cathedral Street, Glasgow G4 0RE, UK
- 18 4. Present address: Francis Crick Institute, 1 Midland Road, King's Cross London,
19 NW1 1AT
- 20 5. Hybrigenics Services, 3 Impasse Reille, 75014 Paris, France
- 21 6. WestCHEM, Department of Pure and Applied Chemistry, University of
22 Strathclyde, Glasgow G1 1XL, UK
- 23 7. Department of Biology, University of Nevada, Reno, NV 89557, USA.

24
25 * First authors contributed equally
26 ‡ Authors for correspondence contributed equally
27 l.machesky@beatson.gla.ac.uk
28 r.insall@beatson.gla.ac.uk

29
30

31 **Abstract**

32

33 Actin-based protrusions are reinforced through positive feedback, but it is
34 unclear what restricts their size, or limits positive signals when they retract or
35 split. We identify an evolutionarily conserved regulator of actin-based
36 protrusion: CYRI (**CY**FIP-related **Rac** i**n**teractor) also known as Fam49. CYRI
37 binds activated Rac1 via a Domain of Unknown Function DUF1394, shared with
38 CYFIP, defining DUF1394 as a Rac1-binding module. CYRI-depleted cells have
39 broad lamellipodia enriched in Scar/WAVE, but reduced protrusion-retraction
40 dynamics. Pseudopods induced by optogenetic Rac1 activation in CYRI-depleted
41 cells are larger and longer-lived. Conversely, CYRI overexpression suppresses
42 recruitment of active Scar/WAVE to the cell edge, resulting in short-lived,
43 unproductive protrusions. CYRI thus focusses protrusion signals and regulates
44 pseudopod complexity by inhibiting Scar/WAVE-induced
45 actin polymerization. It thus behaves like a “local inhibitor” predicted in widely
46 accepted mathematical models, but not previously identified in cells. CYRI
47 therefore regulates chemotaxis, cell migration and epithelial polarisation by
48 controlling polarity and plasticity of protrusions.

49 **Introduction**

50

51 Cell migration is an ancient and fundamental mechanism whereby cells exert
52 control over interactions with their environment. The actin cytoskeleton is the
53 main driver of cell migration, with dozens of proteins controlling actin
54 organisation¹. Actin protrusions, or pseudopods, govern migration, however the
55 feedback loops controlling assembly, splitting and disassembly of these
56 structures is an area of active debate².

57

58 The Scar/WAVE complex is the main driver of Arp2/3-mediated branched actin
59 networks underlying pseudopod generation. The complex consists of five
60 subunits CYFIP, NCKAP1, Scar/WAVE, ABI, HSPC300 (nomenclature in
61 Supplementary Table 1). The main Arp2/3 activating subunit, Scar/WAVE, is
62 autoinhibited until signals trigger a conformational change, exposing an Arp2/3
63 activation sequence^{3,4}. The Scar/WAVE complex is recruited to acidic
64 phospholipids in the plasma membrane via a patch of basic charges³ and via
65 interaction with the small GTPase Rac1⁵⁻⁷.

66

67 Many motile cell types steer by splitting pseudopods into two or more
68 daughters; selecting pseudopods from the split for retraction/maintenance
69 provides a directional bias steering cells up chemotactic gradients⁸. Actin and
70 associated signal transduction networks form excitable systems that propagate
71 in waves and self-limit to drive protrusion and retraction^{1,9,10}. Actin and
72 associated cytoskeletal components likely control their own excitability in
73 concert with signaling lipids, but dynamic interplay between “on” and “off”
74 signals is essential for migration to be plastic and responsive.

75

76 Negative regulators of Arp2/3 complex include Gadkin, which sequesters Arp2/3
77 at the trans Golgi network and endosomes¹¹. Another inhibitor, Arpin mimics
78 the activating sequence of Scar/WAVE but inhibits the Arp2/3 complex¹². Here,
79 we describe a negative regulator of the Scar/WAVE complex, CYRI (encoded by
80 the *FAM49* gene), an evolutionarily conserved protein that mimics the Rac1
81 interaction domain of CYFIP and promotes dynamic pseudopod splitting.

82

83

84 **Results**

85 **CYRI is an evolutionarily conserved N-myristoylated protein with** 86 **homology to CYFIP**

87 We sought new Scar/WAVE complex interactors by precipitating GFP-fused
88 NAP1 (for nomenclature see Supplementary **Table 1**) from *napA* knockout
89 rescued *Dictyostelium* cells. Reversible formaldehyde crosslinking *in cellulo*¹³
90 stabilised transient interactions and GFP-Trap immunocapture recovered
91 Scar/WAVE, ABI, HSPC300 and PIR121. Another interactor was identified as
92 Fam49 (**FAM**ily of unknown function **49**; **Fig 1a** and Supplementary **Table 2**).
93 Although FAM49 did not co-precipitate with the Scar/WAVE complex in the
94 absence of crosslinking, we focused on it for two reasons. Firstly, *FAM49* is
95 highly conserved across evolution and is roughly co-conserved with the
96 Scar/WAVE complex^{14,15} (**Supplementary Fig.1a**). Secondly, Pfam and InterPro
97 identified FAM49 as uniquely sharing a DUF1394 domain with the Scar/WAVE

98 complex subunit CYFIP (**Fig. 1b and Supplementary Fig.1b**). FAM49 proteins
99 comprise mostly DUF1394, while CYFIP proteins contain a cytoplasmic fragile X
100 interaction domain¹⁶ (**Fig. 1b**). We renamed FAM49 to CYRI for **CY**FIP-related
101 **R**ac1 **I**nteractor, in mammals, represented by CYRI-A (FAM49-A) and CYRI-B
102 (FAM49-B) and henceforth we use this nomenclature.

103
104 The DUF1394 region of CYFIP, highlighted in red (PDB 3P8C and **Fig. 1c**) partly
105 overlaps with the published Scar/WAVE complex Rac1 interaction site, in
106 particular R190 in CYFIP³ (**Fig. 1c**, Black arrow and blue balls). Modeling the
107 structure of the DUF1394 of CYRI-B using Phyre2, reveals structural similarities
108 with CYFIP (PDB 3P8C and **Fig. 1d**). The analogous R161 of CYRI (**Fig 1d** blue
109 sidechains, and **e** red box) is part of a highly conserved 33-amino acid stretch
110 (>75% similarity) across diverse phyla (**Supplementary Fig. 1b-c**). R160 is also
111 conserved in CYRI but replaced by lysine in CYFIP (**Fig. 1d-e and**
112 **Supplementary Fig. 1b-c**).

113
114 The N-terminal glycine-2 of CYRI proteins encodes a putative myristoylation
115 site¹⁷⁻¹⁹ (**Fig. 1f**), which is not conserved in CYFIP. We confirmed the
116 myristoylation of CYRI-B by assessing the incorporation of myristate analogue
117 (C14:0-azide) onto G2 using CLICK chemistry *in cellulo*. Mutation of this glycine
118 to alanine abolishes the CLICK signal (**Fig. 1 g-h**).

119
120 In summary, we have defined CYRI, an evolutionarily conserved protein with a
121 putative Rac1-binding DUF1394 module. Furthermore, N-terminal
122 myristoylation suggests CYRI may dynamically associate with the plasma
123 membrane²⁰, where active Rac1 stimulates the Scar/WAVE complex to catalyze
124 lamellipodial expansion.

125
126 **CYRI interacts directly with activated Rac1 *in vitro***
127 Homology between CYRI and CYFIP (**Supplementary Fig. 1b**), suggested
128 potential interaction with Rac1. Yeast two-hybrid screening with Rac1^{G12V} as bait
129 retrieved CYRI-B from multiple cDNA libraries (**Supplementary Fig. 2a**). The
130 core interacting sequence of CYRI-B encompasses amino acids 30-236 (hereafter
131 the Rac Binding Domain - RBD), (**Supplementary Fig. 2b-c**). GFP-RBD expressed
132 in CHL-1 human melanoma cells interacted selectively with GST-Rac1^{Q61L} but not
133 GST-Rac1^{WT}. Mutation of CYRI-B R160 or R161 (in GFP-RBD) to aspartic acid
134 abrogated this interaction (**Fig. 2a-c and Supplementary Fig. 7**). GST-CYRI-B
135 RBD and MBP-Rac1 also showed robust interaction (**Supplementary Fig. 2d-f**
136 **and Supplementary Fig. 7**). In this assay, CYRI does not co-precipitate with
137 Rac1^{T17N}, Rac1^{G12V}, or Rac1^{WT}, likely due to the low affinity of CYRI-B for Rac1.
138 However, the double mutant Rac1^{P29S/Q61L}, recently shown to have a high affinity
139 for the Scar/WAVE complex²¹, displayed enhanced binding to CYRI-B RBD (~3-
140 3.5-fold increase) over Rac1^{Q61L} but no enhanced binding to Pak1-CRIB
141 (**Supplementary Fig. 2 d-f and Supplementary Fig. 7**). Using surface plasmon
142 resonance, immobilised CYRI-B RBD specifically interacted with Rac1^{Q61L} with a
143 K_d of 27 μ M and the reverse assay, with Rac1^{Q61L} immobilised returned a K_d of
144 22 μ M (**Fig. 2g**). As CYRI-RBD shows no homology to CRIB (Cdc42 and Rac
145 interaction binding) motifs, we probed the specificity of the interaction of CYRI
146 between Rac1, RhoA and Cdc42. Once again, CYRI-RBD interacted robustly with

147 Rac1^{Q61L} but not with constitutively active RhoA^{Q63L} or Cdc42^{Q61L} (**Fig. 2d,**
148 **Supplementary Fig. 2g-h and Supplementary Fig. 7**). Thus CYRI-B RBD
149 interacts specifically with active Rac1. Two conserved basic residues in the
150 DUF1394 (conserved in CYFIP) mediate this interaction. This suggests a signal-
151 regulated interaction between active Rac1 and CYRI, similar to the Rac1-CYFIP
152 interaction, defining DUF1394 as an active Rac1 interaction module.

153

154 **CYRI interacts with active Rac1 in cells**

155 We next explored the Rac1-CYRI interaction in cells. Proximity ligation²²
156 revealed an interaction between Rac1^{WT} and CYRI-B in COS-7 cells, as well as a
157 stronger interaction between Rac1^{Q61L} (**Fig. 2h-i and Supplementary Figure 2i-**
158 **l**). Mutation of key arginines in CYRI-B^{R160/161}-HA abolished this interaction and
159 dominant negative Rac1^{T17N} showed no interaction (**Fig. 2 h-i and**
160 **Supplementary Fig. 2i-l**). Targetting either CYRI or Rac1A to mitochondria²³
161 (**Figure 2j**) in *Dictyostelium*, revealed that CYRI^{WT}, but not CYRI mutated for the
162 analogous R155/156D, strongly co-recruits active Rac1A^{P29S/Q61L}. The Pearson's
163 coefficient of fluorescence correlation (PCC) for Rac1A-mCherry-mito and the
164 GFP-fusions revealed a PCC of the positive control CRIB-PBD 0.80 (SD: 0.20 –
165 n=6); CYRI^{WT} 0.77 (SD: 0.21 – n=8 cells); and CYRI^{R155/156D} 0.05 (SD: 0.12 – n=14
166 cells), where 1 = perfect, 0 = no correlation and -1 = excluded. The PCC for Rac1A-
167 mCherry and GFP-mito-fusions were: CRIB-PBD 0.33 (SD: 0.12 – n=6); CYRI^{WT}
168 0.44 (SD: 0.19 – n=12 cells) and CYRI^{R155/156D} -0.23 (SD: 0.05 – n=6 cells). CYRI-
169 GFP did not co-localise with a control mitochondrial reporter mCherry-gemA_{tail}
170 (PCC = -0.06) (SD: 0.15 – n=6 cells). Thus, CYRI interacts with activated Rac1,
171 mediated by key conserved arginines, in both mammalian and *Dictyostelium*
172 cells.

173

174 **CYRI opposes recruitment of the Scar/WAVE complex to lamellipodia**

175 Knockdown or knockout of *CYRI-B* by siRNA or CRISPR in COS-7 or CHL-1 cells
176 did not affect proliferation, but promoted unusually large and broad lamellipodia
177 highly enriched in WAVE2 (**Fig. 3a-b, Supplementary Fig. 3a-g and**
178 **Supplementary Fig. 7**). Cells spread over a larger area and adopted a “fried-
179 egg” phenotype, correlating with an increase in circularity (**Fig. 3c-d,**
180 **Supplementary Fig. 3e-g**). Expression levels of Scar/WAVE complex subunits
181 are not obviously altered in *cyri-b* knockout cells (**Supplementary Fig. 3h and**
182 **Supplementary Fig. 7**). Cell area and circularity were both rescued by re-
183 expression of untagged CYRI-B^{WT}, but not the Rac1-nonbinding R160/161D
184 mutant (**Fig. 3e-f, Supplementary Figure 3i-k and Supplementary Fig. 7**).
185 CYRI-B^{G2A} which cannot be N-myristoylated failed to rescue the phenotype (**Fig.**
186 **3g-h, Supplementary 3l-m and Supplementary Fig. 7**), reinforcing the
187 importance of CYRI lipid modification. *cyri* knockout *Dictyostelium* cells also
188 showed enhanced recruitment of the Scar/WAVE complex (GFP-HSPC300
189 reporter) to a much broader leading edge (**Supplementary Fig. 3n – yellow**
190 **dotted line and Supplementary Movie 1**). Moreover, Scar/WAVE patches in
191 *cyri* knockout cells are ill-defined but longer-lived, suggesting CYRI's ability to
192 suppress Scar/WAVE complex activity outside of active protrusions.
193 (**Supplementary Fig. 3n, heat map**). We conclude that CYRI, via its interaction
194 with active Rac1 and membrane targeting, opposes active Scar/WAVE complex

195 at the plasma membrane and thus drives the formation of more focused and
196 sharper lamellipodial protrusions.

197

198 To determine the requirement for Rac1 for the phenotype of *cyri-b* knockout
199 cells, we co-depleted Rac1 and CYRI-B from mouse tail skin fibroblasts with
200 ROSA26-Cre::ER^{T2+}; *p16Ink4a*^{-/-}; *Rac1*^{n/n} genotype²⁴, treated with
201 hydroxytamoxifen (OHT, to induce deletion of *Rac1*) and then with siRNA against
202 *Cyri-b* (**Supplementary Fig. 3o and Supplementary Fig. 7**). Deletion of *Rac1*
203 led to a spindle-shaped morphology and a loss of lamellipodia as previously
204 described²⁵⁻²⁷. Loss of CYRI-B did not cause excessive lamellipodia or rescue
205 circularity in Rac-deleted cells (**Fig. 3i-k**). Thus, Rac1 is absolutely required for
206 CYRI-B driven actin reorganisation.

207

208 The increased circularity of *cyri-b* depleted cells is reminiscent of Rac1
209 hyperactivation phenotypes²⁸, suggesting that CYRI-B might buffer Rac1 activity.
210 Indeed, a dark acceptor mTq2-sREACH Raichu FRET probe^{29, 30} showed a
211 consistent increase in Rac1 signaling activity in CYRI-B depleted cells, as
212 measured by FRET efficiency in both COS-7 (**Fig. 3l-m**) and CHL-1 cells
213 (**Supplementary Figure 3p-q**), which was confirmed by biochemical pulldown
214 (**Fig. 3n-o and Supplementary Fig. 7**). Together, these data indicate an
215 increase in Rac1 signaling activity in CYRI-B depleted cells. Conversely,
216 inducible overexpression of untagged CYRI-B (**Supplementary Fig. 4a-b and**
217 **Supplementary Fig. 7**) resulted in fractal-like lamellipodia, decreasing WAVE2
218 recruitment, cell area and circularity (**Fig. 4a-d, Supplementary Fig. 4c-f –**
219 **Vehicle-treated controls**). In parallel, overexpression of CYRI-B also drove a
220 decrease in the Rac1 activity signal of the Raichu FRET probe (**Fig. 4e-f**) which
221 was fully reversed by an R160/R161 double mutation (**Fig. 4g**). Thus, CYRI-B
222 opposes Rac1-Scar/WAVE mediated expansion of lamellipodia protrusions.
223 Adding a GFP-tag to either end of CYRI-B interfered with its function, precluding
224 dynamic analysis, likewise, available antibodies to Fam49B did not give specific
225 staining by immunofluorescence, but CYRI-B-FLAG showed significant co-
226 enrichment with WAVE2 at leading pseudopods (**Fig. 4h-i**). Thus CYRI co-
227 accumulates with WAVE2 at lamellipodia protrusions. Overall, *cyri-b* knockout
228 cells show broader Scar/WAVE driven lamellipodia and increased Rac1
229 activation, supporting a role for CYRI-B as a buffer of Rac1 and Scar/WAVE
230 complex activation activity at the leading edges of cells.

231

232 **CYRI regulates the duration and extent of protrusions**

233 We next sought to determine the consequences of CYRI-B depletion for
234 lamellipodial actin dynamics. First, we observed actin dynamics live using fast
235 frame-rate videos in CHL-1 cells expressing GFP-Lifeact (**Fig. 5a – Left panel and**
236 **Supplementary Movie 2**). We tracked the cell edge and used unwrapped
237 (polar) kymographs (**Fig. 5a middle panels**) to visualise and measure the area of
238 protrusion (yellow colour) versus retraction (purple colour) over time. Control
239 cells showed small but rapid bursts of actin-based protrusion (yellow patches on
240 kymograph), while *cyri-b* knockouts had longer-lived less dynamic responses
241 (**Fig. 5a,b**). If CYRI-B buffers Rac1 at the lamellipodium, we speculated that *cyri-b*
242 knockout cells would struggle to restrain protrusion formation upon Rac1
243 activation. To investigate this, we used the Rac1-LOV optogenetic probe, which

244 triggers activation of Rac1 with blue light³¹. Rac1 was activated with pulses of
245 blue light in a discrete area on the cell periphery (**Fig. 5c-d and Supplementary**
246 **Movie 3**). *Cyri-b* knockout cells showed a more sustained and extensive
247 protrusion response and increased peripheral propagation of lamellipodia (**Fig.**
248 **5e-g**). Thus, CYRI-B limits Rac1- mediated activation of the Scar/WAVE complex
249 and shortens the Rac1-activated protrusion.

250

251 **CYRI focuses actin assembly in leading pseudopods to promote plasticity of** 252 **migration**

253 Plasticity of protrusion is important for directional migration, such as during
254 chemotaxis. CHL-1 melanoma cells are normally nearly static when seeded at
255 low density in 2D-culture, but *cyri-b* knockout cells migrated 1.5-2-fold faster
256 (**Fig. 6a-b and Supplementary Movie 4**). *Cyri-b* knockout cells frequently
257 assumed a C-shape, with a broad spread lamellipodium at the front half of the
258 cell and a convex rear which resembled the fast-moving goldfish keratocyte³²
259 (**Supplementary Fig. 5a** yellow arrows, **Supplementary Movie 4**). C-shaped
260 cells moved faster than the other common shapes (**Fig. 6c,d**) and C-shape
261 correlated with faster migration (**Fig. 6e-f and Supplementary Fig. 5b-c**).
262 Lamellipodia need to be polarized and dynamic for efficient cell migration^{27, 33},
263 so when *cyri-b* knockout cells became polarized into a C-shape, they gained
264 motility.

265

266 Since cells need to maintain plasticity of their lamellipodia to respond effectively
267 to directional cues³⁴, we predicted that depletion of CYRI-B would affect
268 chemotactic migration. CHL-1 cells are not chemotactic to serum, but WM852
269 melanoma cells are highly chemotactic³⁵. Loss of CYRI-B (**Supplementary Fig.**
270 **5d-e and Supplementary Fig. 7**) severely affected chemotaxis of these cells
271 towards a 10% serum gradient with no effect on basal speed; Knockouts often
272 migrated very long distances in the opposite direction to the chemoattractant
273 gradient, having lost the plasticity to reorient toward the gradient (**Fig. 6g-i and**
274 **Supplementary Movie 5**). Thus, CYRI-B strongly impacts how cells polarize and
275 remodel their lamellipodia and reorient during directed migration.

276

277 **CYRI promotes pseudopod splitting and opposes persistent migration in** 278 ***Dictyostelium***

279 We examined *Dictyostelium* cells (Ax3, *cyri* knockout and rescue -
280 **Supplementary Fig. 5f and Supplementary Fig. 7**) migrating under agarose up
281 self-generated gradients of the chemoattractant folate³⁶ (**Supplementary Fig.**
282 **5g**). Similar to CHL-1 cells, *cyri* knockout cells were rounder, with blunted
283 pseudopods (**Fig. 6j-k, Supplementary Movies 6-7**). *Dictyostelium* cells
284 primarily turn by splitting their leading pseudopod into differently-oriented
285 daughters⁸; automated segmentation and tracking revealed that *cyri* knockouts
286 generated fewer protrusions/min (**Fig. 6l**) and showed fewer splits (from
287 ~5/min to ~2/min, **Fig. 6m**) and decreased speed (**Fig. 6n**). Cells still oriented
288 towards the folate gradient, but their less efficient turning was clearly reflected
289 by a smaller angle of turn between steps (**Supplementary Fig. 5h**). Thus, CYRI
290 promotes pseudopod splitting in *Dictyostelium* cells, which is dispensible for
291 gradient sensing, but compromises the speed of migration and reorientation
292 while steering.

293
294 We rescued *Dictyostelium cyri* knockouts with CYRI^{WT} or CYRI^{R155/156D} as stable,
295 single-copy transfectants³⁷ under an actin15 promoter (**Fig. 6 j-n,**
296 **Supplementary Movies 6-7**). CYRI^{WT} expressing cells exhibited more
297 numerous fractal pseudopods as well as decreased circularity and enhanced
298 frequency of protrusion generation and pseudopod splitting (**Fig. 6j-m**) even
299 over WT cells. Rescue with CYRI^{WT} also restored cells' ability to turn during
300 chemotaxis (**Supplementary Fig. 5h**).

301
302 Another widely- used chemotaxis assay involves a chemoattractant-filled
303 microneedle introduced just next to *Dictyostelium* cells, inducing new
304 pseudopods directly toward the needle, and consequently reorienting the cells.
305 When cyclic-AMP (cAMP)-sensitive *cyri* knockout or rescue cells were challenged
306 with cAMP in a needle assay, *cyri* knockouts were initially unable to form new
307 pseudopods (**Fig. 6o**), while CYRI^{WT} cells rapidly protruded pseudopods and
308 reoriented toward the needle (**Figure 6o-p and Supplementary Movie 8**). *Cyri*
309 knockouts eventually elongated and streamed toward the needle, but they
310 maintained resistance to new pseudopod formation and rapid reorientation.
311 Thus, cells that lack CYRI can still sense an attractant gradient, but their broad
312 and unfocussed protrusions split rarely, and their diminished ability to generate
313 new pseudopods cripples their response to changing gradients.

314
315
316

317 **Modeling CYRI's role in pseudopod plasticity**

318 Since CYRI affects plasticity of pseudopod dynamics, we likened its activity to the
319 mathematical model of Meinhardt³⁸, where local inhibitors are recruited by an
320 activation signal and limit the amount of cell edge devoted to pseudopods. Actin
321 assembly pathways are not linear cascades, but rather feedback loops where
322 positive stimulation is self-reinforcing and causes further activation until
323 overcome by negative feedback^{4, 10}. In models of migration based around
324 positive feedback, a locally-acting inhibitor is also needed to destabilise existing
325 pseudopods, so the cell can change direction. Without this, cells polarize, but
326 cannot turn to migrate toward an attractant. We used a modified version of a
327 published simulation³⁹ based on the Meinhardt model³⁸ to visualise the
328 concentrations of the activator and the local inhibitor at the cell edge
329 (**Supplementary Fig. 5i and Supplementary Movie 9**), to illustrate the how
330 CYRI-B regulates Rac1 and Scar/WAVE signaling. A peak in the activator (which
331 represents active Rac1 and Scar/WAVE) results in the formation of a new
332 pseudopod. The peak also causes an increase in the concentration of the local
333 inhibitor, which is smaller and thus diffuses faster³⁸. Initially, the inhibitor limits
334 the lateral spread of the pseudopod (**Supplementary Fig. 5i**, panel 1); later,
335 levels of inhibitor rise in the middle of the pseudopod, destabilizing it and
336 causing a split (**Supplementary Fig. 5i**, panel 2). The weaker of the pseudopods
337 then retracts and the stronger is reinforced until the cycle of inhibition catches
338 up with it and re-starts the splitting cycle (**Supplementary Fig. 5i**, panels 3-4).
339 The local inhibitor thus increases both the morphological complexity of the cell
340 and the competition between pseudopods. This is supported by the lack of
341 pseudopod splitting in *Dictyostelium* and our optogenetic data showing that

342 protrusions in *cyri* knockout cells are more long-lived and spread laterally to a
343 greater extent. Thus, Meinhardt's model offers insight into the role of CYRI
344 proteins as local inhibitors, which enhance leading edge dynamics and add
345 plasticity to the positive feedback loops driving migration.

346

347 **CYRI-B regulates epithelial polarity via a Rac1-dependent mechanism**

348 Finally, we tested a role for CYRI-B the polarized epithelial cyst^{40,41} where
349 asymmetric Rac1 activation is also crucial. As cells form a cyst, they establish a
350 lumen via selective membrane trafficking and polarized recruitment/activation
351 of cytoskeletal components⁴². Specific spatial regulation is dependent on matrix
352 and adhesions, but Rac1 activation also regulates lumen formation⁴³ and is
353 specified by differential recruitment of the GEF TIAM1 across the cyst, leading to
354 an apico-basal activation gradient⁴⁰. We hypothesized that CYRI-B might help
355 maintain the Rac1 activation gradient, allowing Scar/WAVE complex
356 recruitment and activation to be spatially controlled during cyst formation.
357 Indeed, knockdown of *CYRI-B* using shRNA in MDCK cells (**Supplementary Fig.**
358 **6a-b and Supplementary Fig. 7**) led to a multilumen phenotype during cyst
359 formation, similar to deregulation of active Rac1 (**Figure 7a-b**,⁴²). WAVE2 is
360 normally prominently localized to the basolateral surfaces of the cysts, but
361 mostly absent from the luminal surface, as marked by podocalyxin (PODXL) (**Fig.**
362 **7c**). However, when CYRI-B was depleted, WAVE2 staining was increased at the
363 luminal periphery coincident with PODXL staining (**Fig. 7c**). Mislocalisation of
364 the actin cytoskeleton machinery to cyst luminal surfaces results in aberrant
365 orientation of the mitotic cleavage plane during polarized cell division, which
366 occurred in *cyri-b* knockdown cysts (**Supplementary Fig. 6c-e**). To test
367 whether the multilumen phenotype was due to inappropriate Rac1 activation,
368 we used moderate concentrations of either EHT1864 (**Fig. 7d-e**) or NSC23766
369 (**Supplementary Fig. 6f**) to dampen Rac1 activity; these both provided a
370 substantial rescue. Thus, loss of CYRI-B destabilised epithelial polarity during
371 the formation of epithelial cell cysts by allowing inappropriate Rac1-mediated
372 recruitment of the actin machinery to the nascent luminal surface. CYRI-B thus
373 maintains spatial regulation of activation of the Scar/WAVE complex by dynamic
374 buffering of Rac1.

375

376 **Discussion**

377 **CYRI is highly conserved and DUF1394 represents a Rac1 interaction** 378 **module**

379 CYRI proteins are highly conserved in eukaryotes and function as a Rac1
380 interaction module that directly limits Rac1-mediated lamellipodia extension.
381 The DUF1394 domain of CYRI comprises the Rac1 binding site and is shared with
382 CYFIP proteins of the Scar/WAVE complex. This interaction requires two highly
383 conserved arginine/lysine residues, previously described on CYFIP1³. CYRI, like
384 CYFIP1, is specific for activated Rac1 over RhoA and Cdc42. Myristoylation of
385 glycine 2 of CYRI may allow recycling of CYRI between active pseudopods and
386 the cytoplasm or membrane vesicles⁴⁴. The Rac1-interacting formin FMNL2 is
387 also myristoylated⁴⁵, implying potential common mechanisms for recruitment to
388 actin protrusions. CYRI has no homology to GTPase activating proteins (GAPs),
389 so it likely doesn't alter nucleotide hydrolysis by Rac1. Why would a cell need
390 CYRI if it has Rac-GAPs? We propose CYRI could be a specific buffer for

391 Scar/WAVE-driven lamellipodia plasticity, rather than a general protein to turn
392 off Rac1.

393

394 **CYRI opposes recruitment of active Scar/WAVE complex to leading edges**
395 **and promotes plasticity**

396

397 Modulating the levels of CYRI differently affected cell speed in the cell types we
398 assayed. While this may seem paradoxical, the basal speeds of these cell types
399 and modes by which they migrate are different. Furthermore, migration speed is
400 multiparametric, being the result of a combination of protrusion, adhesion and
401 directionality/persistence. Migration speed is thought to require optimal levels
402 of Rac1 activation and can be slowed by too little/much active Rac1³³.

403 *Dictyostelium* are optimized by nature to be fast-moving and relatively non-
404 adhesive, so nearly any change will result in slower migration. In contrast, the
405 speed of adhesive slow-moving cancer cells may benefit from removing the
406 brakes on Rac1 activity.

407

408 Negative regulators of Arp2/3 complex have been described^{11, 12, 46}, but thus far,
409 CYRI is the only negative regulator of the Scar/WAVE complex. Importantly, it is
410 widely conserved in evolution along with the Scar/WAVE complex, so is a
411 universal negative regulator. CYRI and CYFIP likely resulted from an ancient
412 gene duplication and retained the same Rac1 binding function, placing CYRI as a
413 Meinhardt local inhibitor³⁸. But a local inhibitor should be present at high
414 enough concentration to compete with the activator. A recent quantitative mass
415 spectrometry study estimated concentrations of CYRI-B to be 4-fold higher in
416 protein copy number than Scar/WAVE complex⁴⁷ in 3 of 4 cell lines (A549 4-
417 fold, HepG2 5-fold, PC3 4.4-fold and U87 0.53-fold, based on comparison with
418 CYFIP1). Thus, there is likely enough CYRI-B in cells to compete with the
419 Scar/WAVE complex for Rac1 binding.

420

421 **CYRI provides spatiotemporal regulation of the connection between Rac1**
422 **and Scar/WAVE complex**

423 Cell migration involves cycles of protrusion and retraction coupled with
424 adhesion to produce forward locomotion⁴⁸. Cells with wild-type levels of CYRI
425 showed rapid protrusion-retraction dynamics indicative of transient activation
426 of the Scar/WAVE complex (e.g. kymograph **Fig. 5a**). *cyri* knockouts showed
427 broader and more sustained lamellipodia and increased Scar/WAVE
428 recruitment, placing CYRI as a key part of the feedback loop controlling leading
429 edge actin dynamics, in line with Arpin, a negative regulator of the Arp2/3
430 complex¹² and coronin, which positively regulates Rac1 activation^{49, 50, 1}.

431 Breaking the feedback loop by deleting CYRI affected both Scar/WAVE
432 recruitment and Rac1 signalling activity. Thus, the actin machinery feeds back to
433 Rac1 dynamically. This dynamic feedback is necessary for cells to change
434 direction and respond with plasticity to stimuli such as chemotactic gradients.

435

436 CYRI also regulates polarized function of Rac1-Scar/WAVE complex in epithelial
437 cells in 3D. Epithelial cells establish a Rac1 gradient that maintains polarity by
438 asymmetric distribution of β 2-syntrophin and Par3⁴⁰. Par3, localized apically,
439 inhibits the Rac-GEF TIAM1, while β 2-syntrophin, localized basally, activates

440 TIAM1. This gradient is required for proper luminogenesis. CYRI helps direct
441 formation of a single polarized lumen by regulating the Rac1 gradient required
442 for proper spindle orientation. A role for CYRI in epithelia could have broad
443 implications for development and cancer.
444

445 Cell migration is the outcome of feedback loops that control the dynamics of cell
446 shapes^{10, 38, 51-53}. Travelling and spreading wave patterns (for example^{10, 51})
447 manifest in actin-based protrusions, implying positive feedback loops. However,
448 negative feedback is also required³⁸ to prevent uniform activation. Actin and
449 actin-binding proteins can comprise an excitable system^{10, 52} also modulated by
450 systems involving small GTPases, kinases and signaling lipids e.g.⁹. Our data
451 imply that CYRI acts at the interface; by competing with Scar/WAVE (an actin-
452 nucleating complex) for Rac1 (a small GTPase) it connects signaling with actin
453 polymerization, moderating excitable behaviours.
454

455 In conclusion, we propose that CYRI is a highly conserved regulator of the
456 dynamics of the Rac1 – Scar/WAVE pathway, providing plasticity and adding
457 complexity to leading edge dynamics.
458

459 **Acknowledgements**

460
461 We thank Margaret O’Prey and the BAIR imaging facility for help with
462 microscopy, Chloe Tesniere for careful work with CYRI overexpression plasmids,
463 Michael Mcilwraith for help with protein purification, Benjamin Tyrell for
464 isolation of the inducible *Rac^{n/n}* fibroblasts, Klemens Rottner and Matthias
465 Schaks for technical advice and discussion, Roland Wedlich-Söldner for the GFP-
466 Lifeact construct. We thank CRUK for core funding to L.M.M. (grant A15673),
467 R.H.I. (grant A19257) and S.Z. (C596/A12935), BBSRC for funding to L.H.C and
468 N.C.O.T (BB/L022087/1), and NIH for funding to G.S.M (NIH RO1 EY025205).
469 Fundação para a Ciência e a Tecnologia, Portugal (PhD scholarship ref.
470 SFRH/BD/69003/2010 awarded to JMB).
471

472 **Author contributions**

473 R.H.I. and J.B. conceived and carried out the initial screen and recognized the
474 similarity of CYRI to CYFIP. L.F. designed and carried out the majority of the
475 experiments on mammalian CYRI-B. L.M.M., R.H.I. and L.F. conceived the study
476 and wrote the paper. P.A.T. designed and constructed the mitochondrial
477 relocalisation tools and carried out the *Dictyostelium* experiments in Figs 2 and
478 6. K.M. and K.I.A. designed the Raichu FRET probe and with L.F. carried out the
479 FRET experiments. P.B. and L.F. carried out the surface plasmon resonance
480 experiments. J.G., N.C.O.T., and L.C. synthesized probes for, advised on and
481 carried out the myristoylation experiments with L.F. S.L. and S.Z. carried out and
482 analysed the mass spectrometry with L.F. and J.B. P.A.T., G.S.M., J.A.W., H.J.S., L.T
483 and S.I. provided essential advice, carried out experiments and analysis of
484 data. M.N. and R.H.I. constructed the model and advised on its use.
485
486

487 Competing interests

488

489 Petra Tafelmeyer works with Hybrigenics, which performs yeast 2-hybrid screening for
490 commercial purposes.

491

492

493 **Figure Legends**

494

495 **Figure 1 - CYRI (Fam49) proteins show homology to CYFIP and contain a** 496 **putative Rac1 interaction motif**

497

498 **a** - Volcano plot illustrating pooled results from four LC-MS/MS experiments
499 showing comparison of formaldehyde crosslinked proteins co-
500 immunoprecipitating with GFP or GFP-NAP1 in *Dictyostelium napA* knockout
501 cells. Color-coding based on two-tailed Welch's t test difference. Curved line is
502 5% false discovery rate. Identified interactors are labeled with gene symbols and
503 presented in **Supplementary Table 2**. (n=4 independent experiments).

504

505 **b** - Schematic of human CYFIP1/2 and CYRI-A/B showing amino acid numbers
506 and domains. Common DUF1394 domain (Pfam PF07159) in red and CYFIP1/2
507 C-terminal cytoplasmic Fragile X Mental Retardation FMR1-interacting domain
508 (FragX-IP, Pfam PF05994) in light green.

509

510 **c** - Two views of ribbon crystal structure of the Scar/WAVE complex (PDB
511 3P8C)². NCKAP1 in lilac, CYFIP1 in light green and red, Scar/WAVE in peach,
512 HSPC300 in yellow and ABI1 in orange. DUF1394 is red, with putative Rac1
513 interaction residues in blue and highlighted by arrows.

514

515 **d** - Phyre prediction of structure of the DUF1394 domain of CYRI-B. The putative
516 Rac1-binding domain of CYRI is blue with Arg160 and Arg161 indicated as a
517 stick representation.

518

519 **e** - Sequence alignment of the putative Rac1-binding domain of CYRI in different
520 organisms. The CYFIP Lys189 and Arg190 equivalent residues are well
521 conserved in CYRI (Arg160 and Arg161) and are highlighted in red.

522

523 **f** - Sequence alignment covering the N-terminal region of CYRI from
524 representative evolutionarily diverse eukaryotes. UniProt accession numbers are
525 reported. Color code represents the number of entries with an identical amino
526 acid at this position. The glycine in the 2nd position (highlighted red) is a putative
527 myristoylation site.

528

529 **g-h** - CLICK chemistry analysis of the glycine 2 of CYRI-B. Myristoylation was
530 labeled in HEK293T cells and measured by incorporation of myristate-azide
531 (green) in GFP, CYRI-B^{WT}-GFP or CYRI-B^{G2A}-GFP mutant transfected cells
532 (magenta), following GFP immunoprecipitation. Molecular markers shown left
533 (**g**) See also **Supplementary Fig. 7 and Supplementary Table 6**. Relative
534 incorporation was quantified by densitometry and reported in (**h**). One way
535 ANOVA with Tukey post-test was applied. *** $p < 0.001$. (n=3 independent
536 assays). Bar graph represents mean and S.E.M.

537 **Figure 2 - CYRI proteins interact with active Rac1**

538

539 **a-c** - Western blot from pulldown of GST control, GST-Rac1^{WT} or GST-
540 Rac1^{Q61L} beads, with cell lysate expressing either GFP alone, positive control
541 PAK1 eCFP-CRIB-PBD, GFP-RBD^{WT}, GFP-RBD^{R160D} or GFP-RBD^{R161D} (**a**).

542 Densitometry (**b-c**). (n=3 independent experiments for GFP-RBD^{R160D} and GFP-
543 RBD^{R161D} and n=4 for GFP and GFP-RBD^{WT}).

544

545 **d-f** - Western blot pulldown of GST control, GST-Rac1^{P29S} or GST-Rac1^{Q61L} or
546 GST-Rac1^{P29S/Q61L} beads, with cell lysate expressing controls or CYRI GFP-RBD^{WT}
547 (**d**). Densitometry (**e-f**). (n=3 independent experiments).

548

549 **g** - Steady state SPR binding curves between Rac1^{Q61L} and CYRI-B-RBD. Left:
550 GST-CYRI-B immobilized vs increasing concentrations of Rac1^{Q61L}. Right: His-
551 Rac1 immobilised vs increasing CYRI-B RBD. Simple 1:1 binding model. K_d =
552 equilibrium dissociation constant, A.U. = arbitrary units.

553

554 **h-i** Proximity ligation assay COS-7 cells on laminin co-expressing CYRI and Rac1
555 constructs. PLA signal (yellow), F-actin (magenta) and nuclei (blue). See
556 **Supplementary Fig. 2** -negative controls. Data pooled across 4 independent
557 experiments in (**i**). One-way ANOVA with Dunn's post-test between CYRI-B^{WT}
558 and MYC-Rac1 constructs. Two-tailed Mann Whitney test between CYRI-B^{WT} and
559 CYRI-B^{R160/161D} for each MYC-Rac1 construct. n.s. $p > 0.05$, ** $p \leq 0.01$, *** $p \leq 0.001$.
560 (anti-HA n=55; anti-Myc n=54; Myc-WT/WT-HA n=55; Myc-WT/R160-161D-HA
561 n=55; Myc-T17N/WT-HA n=63; Myc-T17N/ R160-161D-HA n=84; Myc-
562 Q61L/WT-HA n=69; Myc-Q61L/ R160-161D-HA n=65, where n=cells)
563 Scale bar, 50 μ m.

564

565 **j** - Mitochondrial recruitment of CYRI-GFP to Rac1A-mCherry-mito (Forward) or
566 Rac1A^{P29S/Q61L}-mCherry to CYRI-GFP-mito (Reverse) in Ax3 *D. discoideum*. (>300
567 mitochondria/cell). Far right panels negative control lacking Rac1. Scale bar, 5
568 μ m

569

570 a-j represent at least three biologically independent experiments. Graphs show
571 mean and S.E.M. Source data in **Supplementary Table 6**. Unprocessed Western
572 blots in **Supplementary Figure 7**.

573

574 **Figure 3 - Loss of CYRI-B increases Rac1-mediated Scar/WAVE localisation**
575 **to lamellipodia**

576

577 **a-d** - Immunofluorescence of control (Ctr) or *cyri-b* knockdown (siRNA #1 and 2)
578 COS-7 showing WAVE2 (green), nuclei (blue) and F-actin (magenta). Scale bar =
579 50 μ m. Box insets zoom, scale bar = 10 μ m.

580 Ratio of WAVE2 (yellow dotted line) vs total cell perimeter (**b**). Cell area in (**c**)
581 and circularity (**d**). One-way ANOVA with Dunn's post-test n.s. $p > 0.05$, ***
582 $p \leq 0.001$. (**a-c**: Scramble n=111; #1 n=95; #2 n=96 - **d**: Scramble n=115; #1
583 n=92; #2 n=98) n represents cells in a-o.

584

585 **e-f** -COS-7 with *cyri-b* knockdown and rescued with pLIX-mVenus si-resistant
586 CYRI-B (WT or R160/161D) or empty vector (EV). (see **Supplementary Fig. 3I**).
587 Cell area (**e**) and circularity (**f**). One-way ANOVA with Dunn's post-test n.s. $p >$
588 0.05, *** $p \leq 0.001$. (Scramble/EV n=78; Scramble/WT n=58; Scramble/R160-
589 161D n=66; #1/EV n=66; #1/WT n=64; #1/R160-161D n=60).

590

591 **g-h** - Control or *cyri-b* knockdown COS-7 with pLIX-mVenus and si-resistant
592 CYRI-B (WT or G2A mutant) or EV. Cell area (**g**) and circularity (**h**). One-way
593 ANOVA with Dunn's post-test n.s. $p > 0.05$, *** $p \leq 0.001$. (Scramble/EV n=70;
594 Scramble/WT n=52; Scramble/G2A n=46; #1/EV n=63; #1/WT n=64; #1/G2A
595 n=65)

596

597 **i-k** - Control (DMSO) or *rac1* knockout (OHT) mouse tail fibroblasts with
598 Scramble (siCtr) or *Cyri-B* siRNA, showing WAVE2 (**i**). Scale bar = 50 μ m.
599 Lamellipodial WAVE2 (**j**) and circularity (**k**). One-way ANOVA with Dunn's post-
600 test *** $p \leq 0.001$. two-tailed Mann Whitney test between OHT and control. ###
601 $p \leq 0.001$. (n=30 cells/condition).

602

603 **l-m** - FLIM/FRET of mTq2-sREACH in control (siCtr) or *cyri-b* knockdown
604 (siCYRI-B #1 and #2) COS-7. Jet2 color code (left) average lifetime, 1-4 ns blue to
605 red. (**l**). FRET efficiency (**m**). One-way ANOVA with Dunn's post-test. *** $p \leq 0.001$.
606 (Scramble n=61; #1 n=61, #2 n=63)

607 Scale bar = 50 μ m

608

609 **n-o** - Active Rac1 pulldown comparing control CrispR (Vector^{Ctr}) or independent
610 *cyri-b* CrispR (#1 and #2) COS-7 lines. See also Supplementary Fig. 7.

611

612 Data in a-o represent three biologically independent experiments. All cells
613 plated on laminin. See also Supplementary Table 6.

614 Bar and scatter plots show data points with mean and S.E.M.

615 Whisker plots show 10-90 percentile, median (bar) and mean (cross).

616

617 **Figure 4 - Overexpression of CYRI-B opposes Rac1-mediated Scar/WAVE**
618 **recruitment to the leading edge**

619

620 **a-d** - Immunofluorescence of doxycycline-induced control empty vector (EV) or
621 CYRI-B overexpression in COS-7 cells and fixed after 4h showing WAVE2
622 (magenta), nuclei (blue) and GFP (green). Scale bar = 50 μm . Insets show zoom
623 of white dashed field. Scale bar = 10 μm (**a**). WAVE2 ratio and circularity in (**b**)
624 and (**c**) respectively. Cell area quantification was based on phalloidin staining
625 (**d**). Two-tailed Mann-Whitney test *** $p \leq 0.001$. (Dox/EV n=73; Dox/CYRI-B
626 n=93) n represents cells in a-i

627

628 **e-f** - FLIM/FRET experiment with mTq2-sREACH Raichu Rac1 showing vehicle
629 or doxycycline-treated COS-7 cells expressing a control empty vector (EV) or
630 CYRI-B. The jet2 color code (bar at top) shows the average lifetime of the probe,
631 spanning 1-4 ns (blue to red) (**e**). Quantification of the FRET efficiency (**f**). Two-
632 tailed Mann-Whitney test n.s. $p > 0.05$, *** $p \leq 0.001$. (Veh/EV n=47; Veh/CYRI-B
633 n=46; Dox/EV n=62; Dox/CYRI-B n=62)
634 Scale bar = 50 μm .

635

636 **g** - FRET efficiency obtained from control (EV) or COS-7 cells overexpressing
637 CYRI^{WT} or CYRI-B^{R160/161D} after doxycycline induction. One-way ANOVA with
638 Dunn's post-test was performed. n.s. $p > 0.05$, *** $p \leq 0.001$. (EV n=59; WT n=62;
639 R160/161D n=63).

640 **h-i** - Immunofluorescence of COS-7 cells transfected with CYRI-B-FLAG and
641 stained for FLAG-tag (green), F-actin (top row) or WAVE2 (bottom row)
642 (magenta) and nuclei (blue). Scale bar = 50 μm (**h**). FLAG-staining is
643 quantified by normalizing the fluorescence intensity running across 17
644 representative cells and ending at the protrusive end (normalized distance:
645 1=protrusive end and 0=opposite end). FLAG-tag and F-actin staining
646 intensity are shown in green and magenta respectively (**i**) (n=17).

647

648

649 Data in a-i represent three biologically independent experiments.

650 See also Supplementary Table 6.

651 Bar and scatter plots show data points with mean and S.E.M.

652 Whisker plots show 10-90 percentile, median (bar) and mean (cross).

653

654

655 **Figure 5 - CYRI-B controls the duration and extent of Rac1-mediated**
656 **protrusions**

657

658 **a** - Control (Vector^{Ctrl}) and *cyri-b* CrispR knockout CHL-1 cells on laminin
659 expressing GFP-LifeAct, recorded for 3 minutes at 1 frame/sec. The cell
660 periphery (magenta) is tracked using the GFP-LifeAct signal (green) (Left panel).
661 The membrane is unravelled from the orange arrow and a representative polar
662 kymograph of the changes in membrane dynamics over time between control
663 (Vector^{Ctrl} - Top) and *cyri-b* CrispR knockout (Bottom) CHL-1 cells is shown.
664 Membrane extensions (positive values) are visualised in yellow through to
665 orange, while retractions (negative values) are purple-blue (Middle
666 panel). Thresholding of the kymograph to remove noise (values $\geq + 0.6$) reveals
667 protrusions over time (white signal - Right panel)
668 Still from movie S2. Scale bar = 25 μm .

669

670 **b** - Box plot representing the distribution of the average protrusion lifetime for
671 each individual cell. Whisker plots represent mean and S.D. Two-tailed Mann
672 Whitney test. *** $p \leq 0.001$. (n= 20 cells/condition)

673

674 **c** - Schematic representation showing protruding (blue) and retracting
675 (magenta) area following photoactivation of Rac1-LOV probe. Photo activation
676 area (green circle) was used as the origin to measure the maximal protrusion
677 distance (outward - black line) and the longest uninterrupted lateral spread of
678 the protrusion (red dotted line)

679

680 **d** - Still pictures from videos of photoactivation time course showing selected
681 cells from DMSO (Control) or OHT-treated (knockout) immortalized CRE-ER^{T2+}
682 *Cyri-B^{fl/fl}* MEFs on fibronectin. Endpoint overlay as from schematic (c). Scale bar
683 = 25 μm .

684

685 **e-f** - Quantification of the protrusion distance (**e**) and the spread of activation (**f**)
686 between control (DMSO) or *cyri-b* knockout (OHT) MEFs.
687 Error bars represent 95% CI. Unpaired two-tailed t-test (**e**) and two-tailed
688 Mann-Whitney test (**f**). *** $p \leq 0.001$, **** $p \leq 0.0001$. (DMSO n=29 cells; OHT n=30
689 cells).

690

691 **g** - Kymograph representation before and after photo activation. Membrane
692 extensions are visualised in yellow through to orange, while retractions are
693 observed in purple-blue. Time of photoactivation is highlighted by a white dotted
694 line.

695

696 Data in a-g represent three biologically independent experiments.

697 See also Supplementary Table 6.

698

699 **Figure 6 - CYRI modulates protrusion plasticity during directional**
700 **migration**

701

702 **a-c** - Spider plots CrispR and control CHL-1 cells on collagen-I, 17h (**a**) (See
703 **movie S4**). Black and red lines = distance > or <100 μm respectively. Average
704 speed (**b**). (**c**) Duration as C-shape (**b,c**) One-way ANOVA with Dunn's post-test
705 (**b**) (Ctr n=161; #1 n=228; #2 n=178). (**c**) (Ctr n=45; #1 n=53; #2 n=42). n=cells
706 in a-p.

707

708 **d** - Speed of CrispR and control CHL-1. One-way ANOVA with Dunn's post-test
709 (Ctr n=45; #1 n=53; #2 n=42)

710

711 **e-f** - Immunofluorescence of CrispR and control CHL-1 on collagen. F-actin
712 (magenta) and nuclei (blue) (**e**). Scale bar = 50 μm . (**f**). Two-tailed Chi-square
713 test (95% confidence). (Ctr n=276; #1 n=216; #2 n=210)

714

715 **g-i** - Spider and Rose plots of CrispR and control WM852 cell chemotaxis (**g**) (see
716 **movie S5**). Red-dashed lines 95% confidence interval for mean direction. Cos θ
717 (chemotactic index) (**h**) average speed (**i**). Two-tailed unpaired t-test. (Ctr
718 n=129; #1 n=132; #2 n=151).

719

720 **j-n** - DIC pictures from *Dictyostelium* under-agarose chemotaxis (**j**) (see **movie**
721 **S6**). Scale bar = 10 μm . Circularity (**k**), protrusions (**l**), split frequency (**m**), and
722 speed (**n**). One-way ANOVA with Dunn's post-test. (**k**: WT n=360; *cyri* KO n=352;
723 *cyri* KO + CYRI^{WT} n=480; *cyri* KO + CYRI^{R155/156} n=240 - **l**: WT n=45; *cyri* KO
724 n=57; *cyri* KO + CYRI^{WT} n=53; *cyri* KO + CYRI^{R155/156} n=31 - **m**: WT n=42; *cyri* KO
725 n=62; *cyri* KO + CYRI^{WT} n=46; *cyri* KO + CYRI^{R155/156} n=33 - **n**: WT n=2389; *cyri*
726 KO n=2460; *cyri* KO + CYRI^{WT} n=3024; *cyri* KO + CYRI^{R155/156} n=1169)

727

728 **o-p** - Needle assay using WT or *cyri* knockout Ax3 cells with cAMP (see also
729 **movie S8**) (yellow start). Scale bar = 25 μm (**o**). Spider plots during 0-100s (**p**).
730 (WT n=86; *cyri* KO n=79)

731

732 a-p represent three biologically independent experiments with mean and S.E.M
733 unless indicated. Whisker plots 10-90 percentile (**b**, **k-m**) and 1-99 percentile
734 (**n**) with median (bar) and mean (cross). n.s. $p>0.05$, * $p\leq 0.05$, ** $p\leq 0.01$, ***
735 $p\leq 0.001$.

736 See Supplementary Table 6.

737

738 **Figure 7 - CYRI-B regulates Rac1-dependent recruitment of Scar/WAVE**
739 **complex during epithelial cystogenesis**

740

741 **a-b** - Immunofluorescence of control (Vector^{Ctrl}) or *cyri-b* shRNA knockdown
742 (#1 and #2) MDCK cysts fixed after 5 days of culture and stained for Podocalyxin
743 (PODXL) (green), F-actin (red) and nuclei (blue). Top row is a confocal section
744 and bottom row represents Z-maximal projection intensity of PODXL staining.
745 Scale bar = 50 μm (**a**). Quantification of lumens in (**b**). One-way ANOVA with
746 Dunn's post-test. *** $p < 0.001$. (Ctr n=1000 cysts, #1 n=1000 cysts, #2 n=800
747 cysts).

748 **c** - Immunofluorescence of control (Vector^{Ctrl}) or *cyri-b* shRNA knockdown (#1
749 and #2) MDCK cysts stained for WAVE2 (green) and Podocalyxin (PODXL) (red)
750 after 5 days of culture. Inverted LUT images, merge and representative surface
751 profile plots shown. PODXL (red) and WAVE2 (green) staining intensity was
752 measured along the blue line. Scale bar = 9 μm . Insets provide a magnified view
753 of the dotted square area. Scale bar = 5 μm .

754 **d-e** - Immunofluorescence of control (Vector^{Ctrl}) or *cyri-b* shRNA knockdown
755 (#1 and #2) MDCK cysts grown during 5 days, treated or not with 50 nM
756 EHT1864 and stained for Podocalyxin (PODXL). Pictures represent the Z-
757 maximal projection intensity from a representative z-stack running across the
758 entire cyst volume. Scale bar = 50 μm (**d**). Number of lumens per cyst was
759 quantified for vehicle or EHT1864-treated cysts and plotted in (**e**). One-way
760 ANOVA with Dunn's post-test between control (Vector^{Ctrl}), shCYRI-B #1 and
761 shCYRI-B #2 whereas unpaired two-tailed t-test between vehicle and drug-
762 treated cyst. n.s. $p > 0.05$, ** $p \leq 0.01$ *** $p \leq 0.001$. (250 cysts/condition)

763 Data in a-e represent N=3 biologically independent experiments.

764 Bar and scatter plots show data points with mean and S.E.M.

765 Whisker plots show 10-90 percentile, median (bar) and mean (cross).

766 See also Supplementary Table 6.

767

768 **References**

769

770

771

- 772 1. Krause, M. & Gautreau, A. Steering cell migration: lamellipodium
773 dynamics and the regulation of directional persistence. *Nat Rev Mol Cell*
774 *Biol* **15**, 577-590 (2014).
- 775 2. Insall, R. The interaction between pseudopods and extracellular signalling
776 during chemotaxis and directed migration. *Curr Opin Cell Biol* **25**, 526-531
777 (2013).
- 778 3. Chen, Z. *et al.* Structure and control of the actin regulatory WAVE
779 complex. *Nature* **468**, 533-538 (2010).
- 780 4. Davidson, A.J. & Insall, R.H. Actin-based motility: WAVE regulatory
781 complex structure reopens old SCARs. *Curr Biol* **21**, R66-68 (2011).
- 782 5. Hoeller, O. *et al.* Gbeta Regulates Coupling between Actin Oscillators for
783 Cell Polarity and Directional Migration. *PLoS Biol* **14**, e1002381 (2016).

- 784 6. Veltman, D.M., King, J.S., Machesky, L.M. & Insall, R.H. SCAR knockouts in
785 Dictyostelium: WASP assumes SCAR's position and upstream regulators
786 in pseudopods. *J Cell Biol* **198**, 501-508 (2012).
- 787 7. Weiner, O.D. *et al.* Hem-1 complexes are essential for Rac activation, actin
788 polymerization, and myosin regulation during neutrophil chemotaxis.
789 *PLoS Biol* **4**, e38 (2006).
- 790 8. Andrew, N. & Insall, R.H. Chemotaxis in shallow gradients is mediated
791 independently of PtdIns 3-kinase by biased choices between random
792 protrusions. *Nat Cell Biol* **9**, 193-200 (2007).
- 793 9. Devreotes, P.N. *et al.* Excitable Signal Transduction Networks in Directed
794 Cell Migration. *Annu Rev Cell Dev Biol* **33**, 103-125 (2017).
- 795 10. Graziano, B.R. & Weiner, O.D. Self-organization of protrusions and polarity
796 during eukaryotic chemotaxis. *Curr Opin Cell Biol* **30**, 60-67 (2014).
- 797 11. Maritzen, T. *et al.* Gadkin negatively regulates cell spreading and motility
798 via sequestration of the actin-nucleating ARP2/3 complex. *Proc Natl Acad*
799 *Sci U S A* **109**, 10382-10387 (2012).
- 800 12. Dang, I. *et al.* Inhibitory signalling to the Arp2/3 complex steers cell
801 migration. *Nature* **503**, 281-284 (2013).
- 802 13. Sobczyk, G.J., Wang, J. & Weijer, C.J. SILAC-based proteomic quantification
803 of chemoattractant-induced cytoskeleton dynamics on a second to minute
804 timescale. *Nat Commun* **5**, 3319 (2014).
- 805 14. Keeling, P.J. *et al.* The tree of eukaryotes. *Trends Ecol Evol* **20**, 670-676
806 (2005).
- 807 15. Veltman, D.M. & Insall, R.H. WASP family proteins: their evolution and its
808 physiological implications. *Mol Biol Cell* **21**, 2880-2893 (2010).
- 809 16. Bramham, C.R., Jensen, K.B. & Proud, C.G. Tuning Specific Translation in
810 Cancer Metastasis and Synaptic Memory: Control at the MNK-eIF4E Axis.
811 *Trends Biochem Sci* **41**, 847-858 (2016).
- 812 17. Bienvenut, W.V. *et al.* Comparative large scale characterization of plant
813 versus mammal proteins reveals similar and idiosyncratic N-alpha-
814 acetylation features. *Mol Cell Proteomics* **11**, M111 015131 (2012).
- 815 18. Broncel, M. *et al.* Multifunctional reagents for quantitative proteome-wide
816 analysis of protein modification in human cells and dynamic profiling of
817 protein lipidation during vertebrate development. *Angew Chem Int Ed*
818 *Engl* **54**, 5948-5951 (2015).
- 819 19. Yang, W., Di Vizio, D., Kirchner, M., Steen, H. & Freeman, M.R. Proteome
820 scale characterization of human S-acylated proteins in lipid raft-enriched
821 and non-raft membranes. *Mol Cell Proteomics* **9**, 54-70 (2010).
- 822 20. Lanyon-Hogg, T., Faronato, M., Serwa, R.A. & Tate, E.W. Dynamic Protein
823 Acylation: New Substrates, Mechanisms, and Drug Targets. *Trends*
824 *Biochem Sci* (2017).
- 825 21. Chen, B. *et al.* Rac1 GTPase activates the WAVE regulatory complex
826 through two distinct binding sites. *Elife* **6** (2017).
- 827 22. Soderberg, O. *et al.* Characterizing proteins and their interactions in cells
828 and tissues using the in situ proximity ligation assay. *Methods* **45**, 227-
829 232 (2008).
- 830 23. Robinson, M.S., Sahlender, D.A. & Foster, S.D. Rapid inactivation of
831 proteins by rapamycin-induced rerouting to mitochondria. *Dev Cell* **18**,
832 324-331 (2010).

- 833 24. Walmsley, M.J. *et al.* Critical roles for Rac1 and Rac2 GTPases in B cell
834 development and signaling. *Science* **302**, 459-462 (2003).
- 835 25. Li, A. *et al.* Activated mutant NRas(Q61K) drives aberrant melanocyte
836 signaling, survival, and invasiveness via a Rac1-dependent mechanism. *J*
837 *Invest Dermatol* **132**, 2610-2621 (2012).
- 838 26. Li, A. *et al.* Rac1 drives melanoblast organization during mouse
839 development by orchestrating pseudopod- driven motility and cell-cycle
840 progression. *Dev Cell* **21**, 722-734 (2011).
- 841 27. Steffen, A. *et al.* Rac function is crucial for cell migration but is not
842 required for spreading and focal adhesion formation. *J Cell Sci* **126**, 4572-
843 4588 (2013).
- 844 28. Ridley, A.J., Paterson, H.F., Johnston, C.L., Diekmann, D. & Hall, A. The small
845 GTP-binding protein rac regulates growth factor-induced membrane
846 ruffling. *Cell* **70**, 401-410 (1992).
- 847 29. Martin, K.J. *et al.* Accepting from the best donor; analysis of long-lifetime
848 donor fluorescent protein pairings to optimise dynamic FLIM-based FRET
849 experiments. *PLoS One* **13**, e0183585 (2018).
- 850 30. Nakamura, T., Kurokawa, K., Kiyokawa, E. & Matsuda, M. Analysis of the
851 spatiotemporal activation of rho GTPases using Raichu probes. *Methods*
852 *Enzymol* **406**, 315-332 (2006).
- 853 31. Wu, Y.I. *et al.* A genetically encoded photoactivatable Rac controls the
854 motility of living cells. *Nature* **461**, 104-108 (2009).
- 855 32. Keren, K., Yam, P.T., Kinkhabwala, A., Mogilner, A. & Theriot, J.A.
856 Intracellular fluid flow in rapidly moving cells. *Nat Cell Biol* **11**, 1219-
857 1224 (2009).
- 858 33. Pankov, R. *et al.* A Rac switch regulates random versus directionally
859 persistent cell migration. *J Cell Biol* **170**, 793-802 (2005).
- 860 34. Insall, R. & Andrew, N. Chemotaxis in Dictyostelium: how to walk straight
861 using parallel pathways. *Curr Opin Microbiol* **10**, 578-581 (2007).
- 862 35. Muinonen-Martin, A.J. *et al.* Melanoma cells break down LPA to establish
863 local gradients that drive chemotactic dispersal. *PLoS Biol* **12**, e1001966
864 (2014).
- 865 36. Tweedy, L., Knecht, D.A., Mackay, G.M. & Insall, R.H. Self-Generated
866 Chemoattractant Gradients: Attractant Depletion Extends the Range and
867 Robustness of Chemotaxis. *PLoS Biol* **14**, e1002404 (2016).
- 868 37. Kuspa, A. & Loomis, W.F. Tagging developmental genes in Dictyostelium
869 by restriction enzyme-mediated integration of plasmid DNA. *Proc Natl*
870 *Acad Sci U S A* **89**, 8803-8807 (1992).
- 871 38. Meinhardt, H. Orientation of chemotactic cells and growth cones: models
872 and mechanisms. *J Cell Sci* **112 (Pt 17)**, 2867-2874 (1999).
- 873 39. Neilson, M.P., Mackenzie, J.A., Webb, S.D. & Insall, R.H. Use of the
874 parameterised finite element method to robustly and efficiently evolve
875 the edge of a moving cell. *Integr Biol (Camb)* **2**, 687-695 (2010).
- 876 40. Mack, N.A. *et al.* beta2-syntrophin and Par-3 promote an apicobasal Rac
877 activity gradient at cell-cell junctions by differentially regulating Tiam1
878 activity. *Nat Cell Biol* **14**, 1169-1180 (2012).
- 879 41. Mangan, A.J. *et al.* Cingulin and actin mediate midbody-dependent apical
880 lumen formation during polarization of epithelial cells. *Nat Commun* **7**,
881 12426 (2016).

- 882 42. Overeem, A.W., Bryant, D.M. & van, I.S.C. Mechanisms of apical-basal axis
883 orientation and epithelial lumen positioning. *Trends Cell Biol* **25**, 476-485
884 (2015).
- 885 43. Yagi, S., Matsuda, M. & Kiyokawa, E. Suppression of Rac1 activity at the
886 apical membrane of MDCK cells is essential for cyst structure
887 maintenance. *EMBO Rep* **13**, 237-243 (2012).
- 888 44. Jiang, H. *et al.* Protein Lipidation: Occurrence, Mechanisms, Biological
889 Functions, and Enabling Technologies. *Chem Rev* **118**, 919-988 (2018).
- 890 45. Grobe, H., Wustenhagen, A., Baarlink, C., Grosse, R. & Grikscheit, K. A Rac1-
891 FMNL2 signaling module affects cell-cell contact formation independent
892 of Cdc42 and membrane protrusions. *PLoS One* **13**, e0194716 (2018).
- 893 46. Madasu, Y. *et al.* PICK1 is implicated in organelle motility in an Arp2/3
894 complex-independent manner. *Mol Biol Cell* **26**, 1308-1322 (2015).
- 895 47. Wisniewski, J.R., Hein, M.Y., Cox, J. & Mann, M. A "proteomic ruler" for
896 protein copy number and concentration estimation without spike-in
897 standards. *Mol Cell Proteomics* **13**, 3497-3506 (2014).
- 898 48. Meacci, G. *et al.* alpha-Actinin links extracellular matrix rigidity-sensing
899 contractile units with periodic cell-edge retractions. *Mol Biol Cell* **27**,
900 3471-3479 (2016).
- 901 49. Swaminathan, K., Muller-Taubenberger, A., Faix, J., Rivero, F. & Noegel,
902 A.A. A Cdc42- and Rac-interactive binding (CRIB) domain mediates
903 functions of coronin. *Proc Natl Acad Sci U S A* **111**, E25-33 (2014).
- 904 50. Swaminathan, K. *et al.* Coronin7 regulates WASP and SCAR through CRIB
905 mediated interaction with Rac proteins. *Sci Rep* **5**, 14437 (2015).
- 906 51. Gerisch, G. *et al.* Mobile actin clusters and traveling waves in cells
907 recovering from actin depolymerization. *Biophys J* **87**, 3493-3503 (2004).
- 908 52. Killich, T. *et al.* The locomotion, shape and pseudopodial dynamics of
909 unstimulated Dictyostelium cells are not random. *J Cell Sci* **106 (Pt 4)**,
910 1005-1013 (1993).
- 911 53. Tweedy, L., Susanto, O. & Insall, R.H. Self-generated chemotactic
912 gradients-cells steering themselves. *Curr Opin Cell Biol* **42**, 46-51 (2016).
- 913

Figure 1

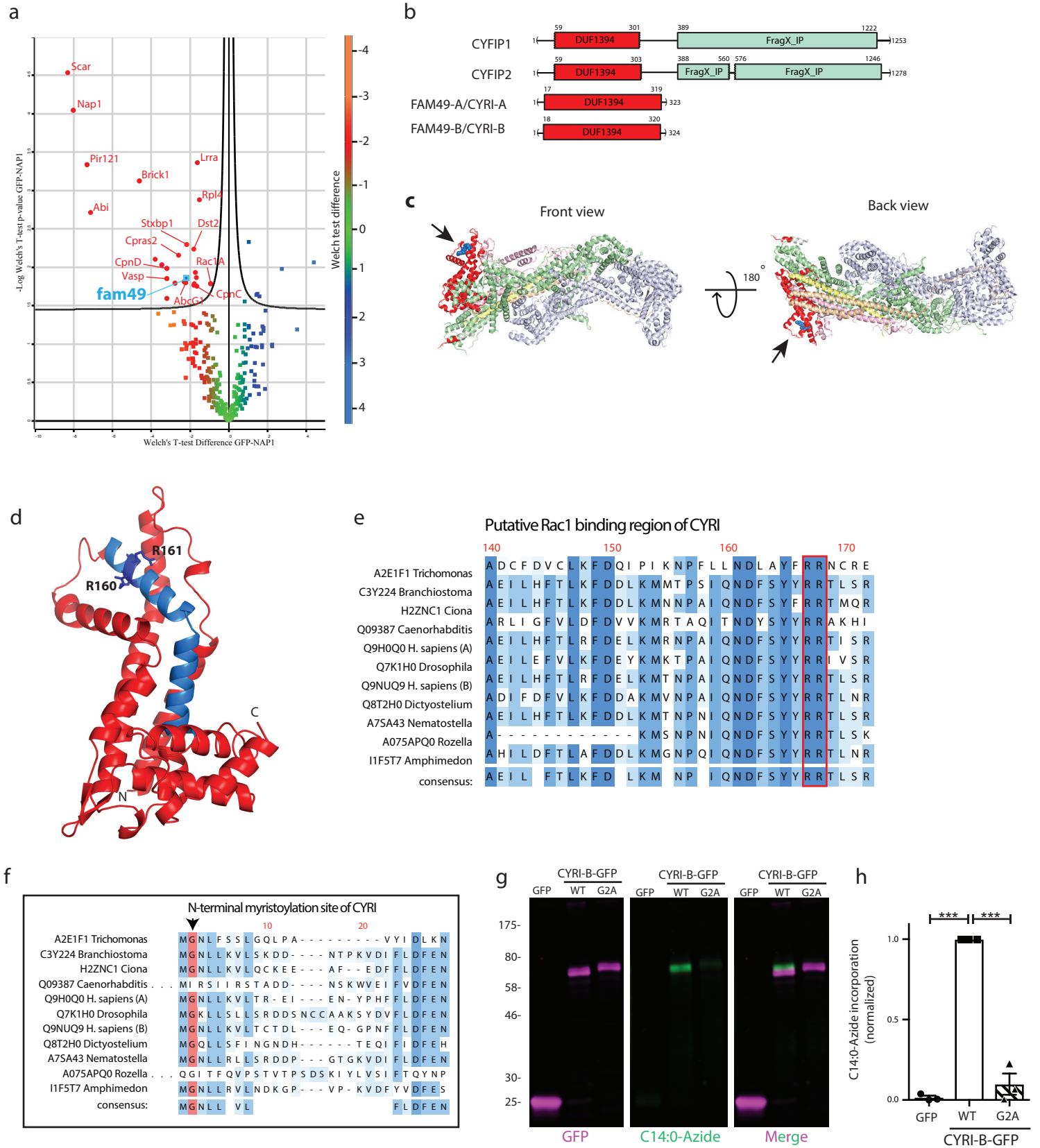


Figure 2

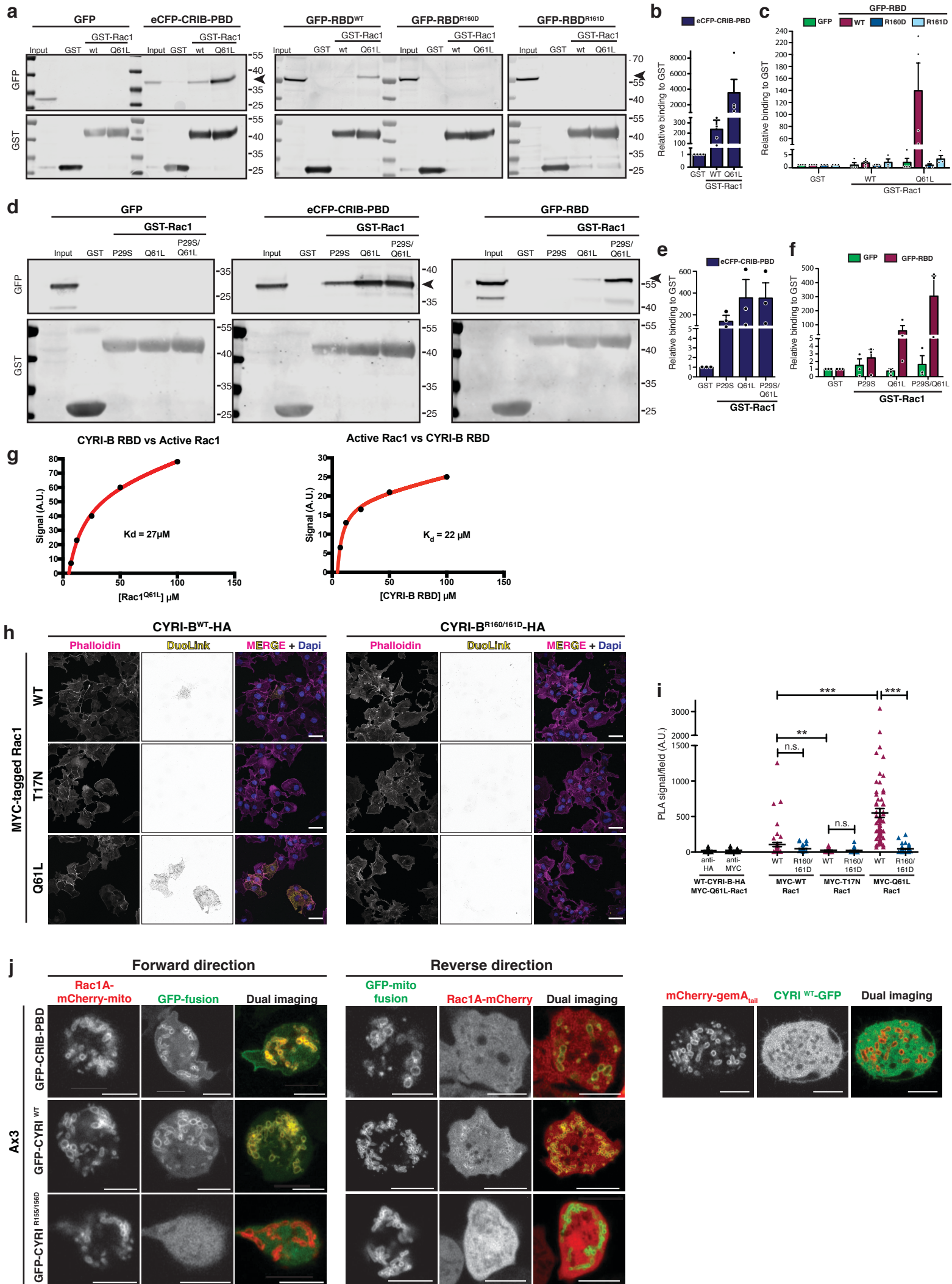


Figure 3

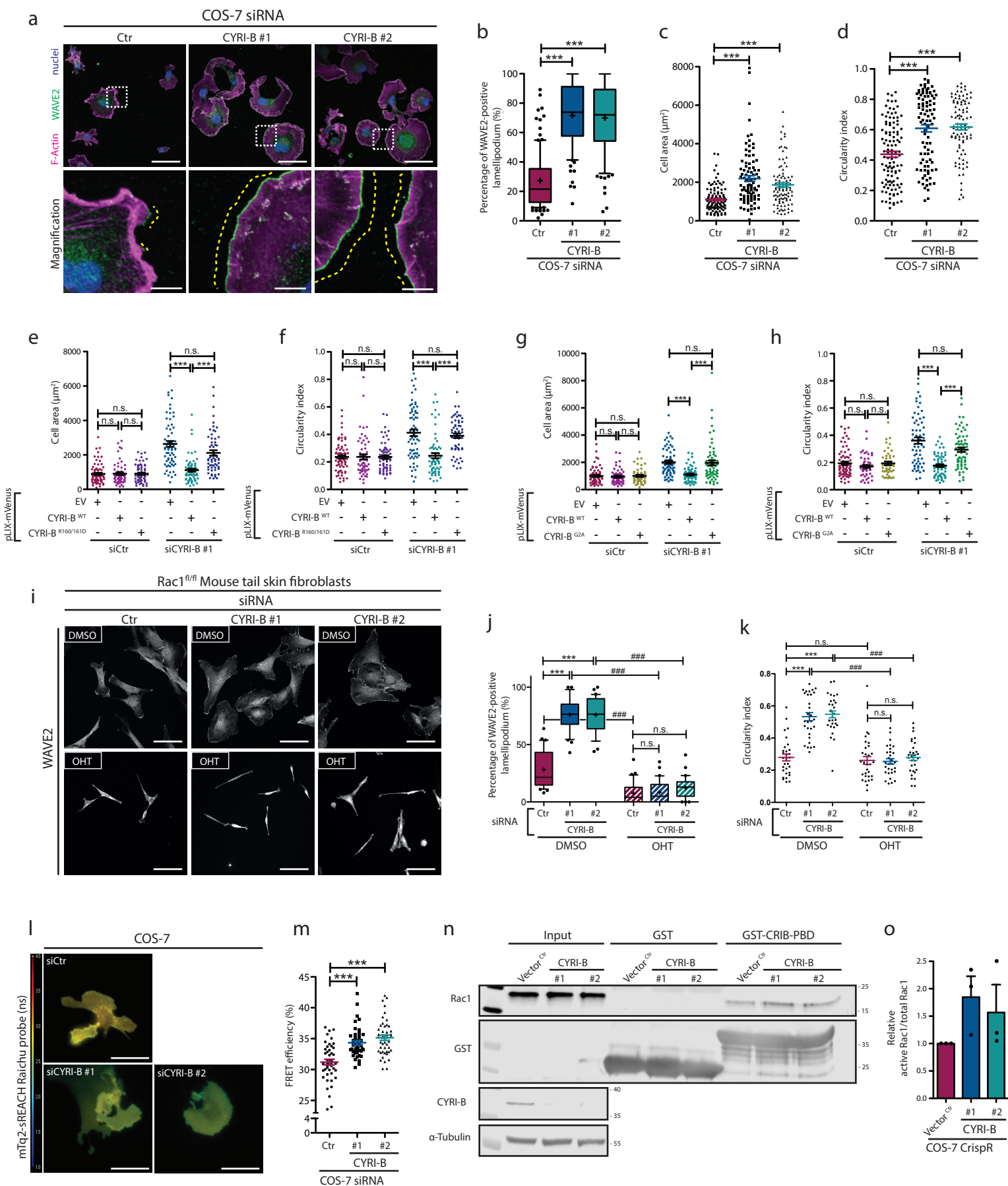


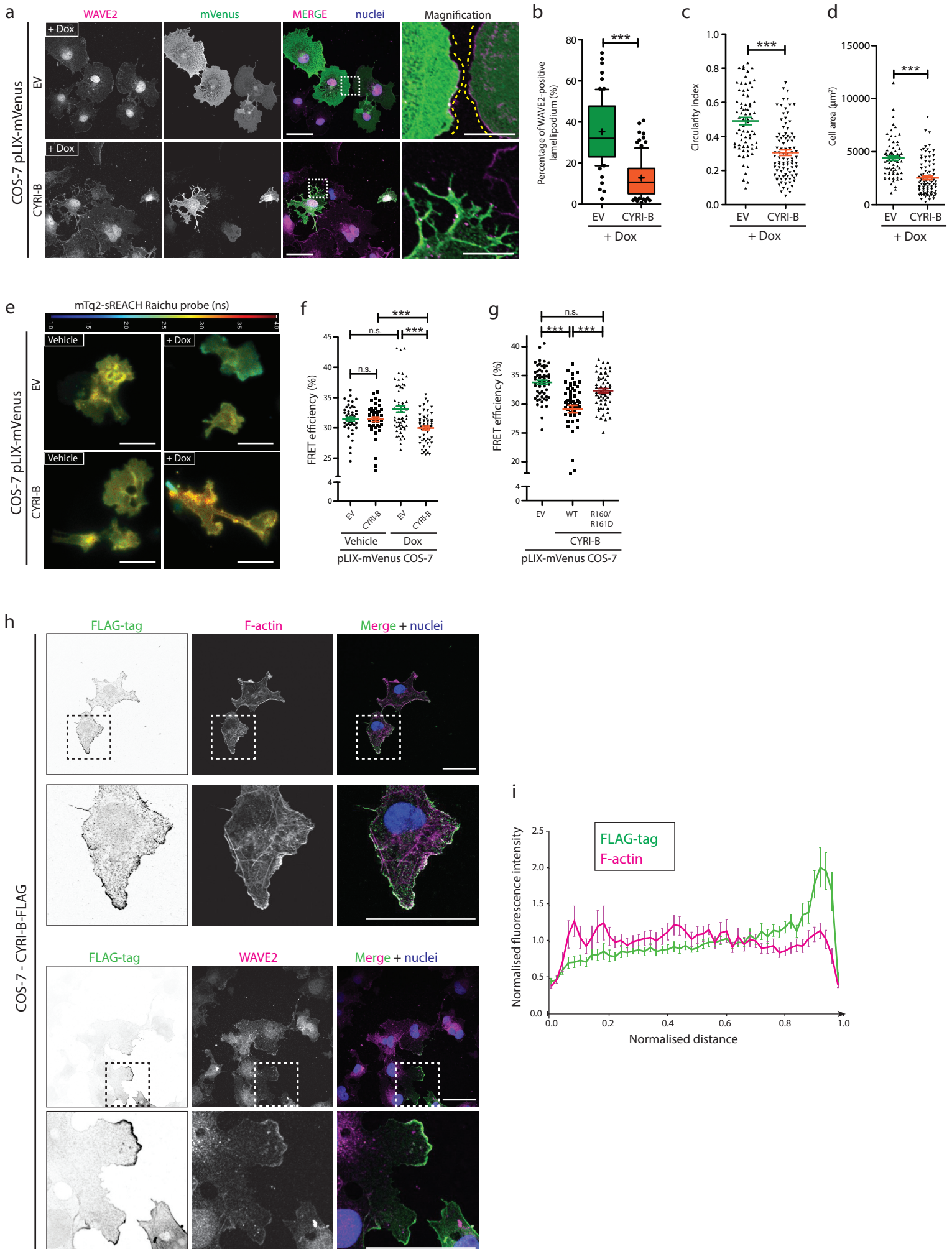
Figure 4

Figure 5

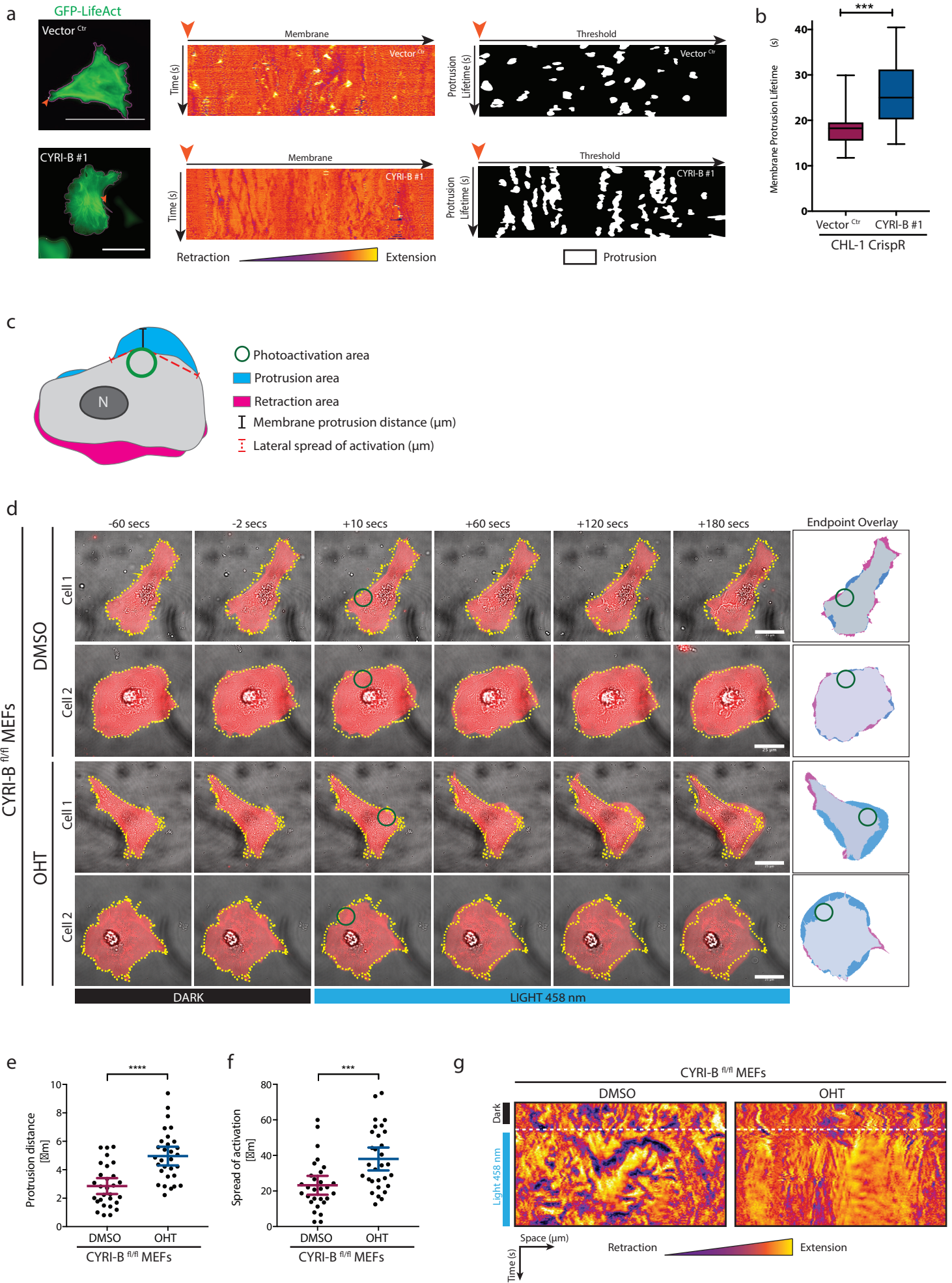


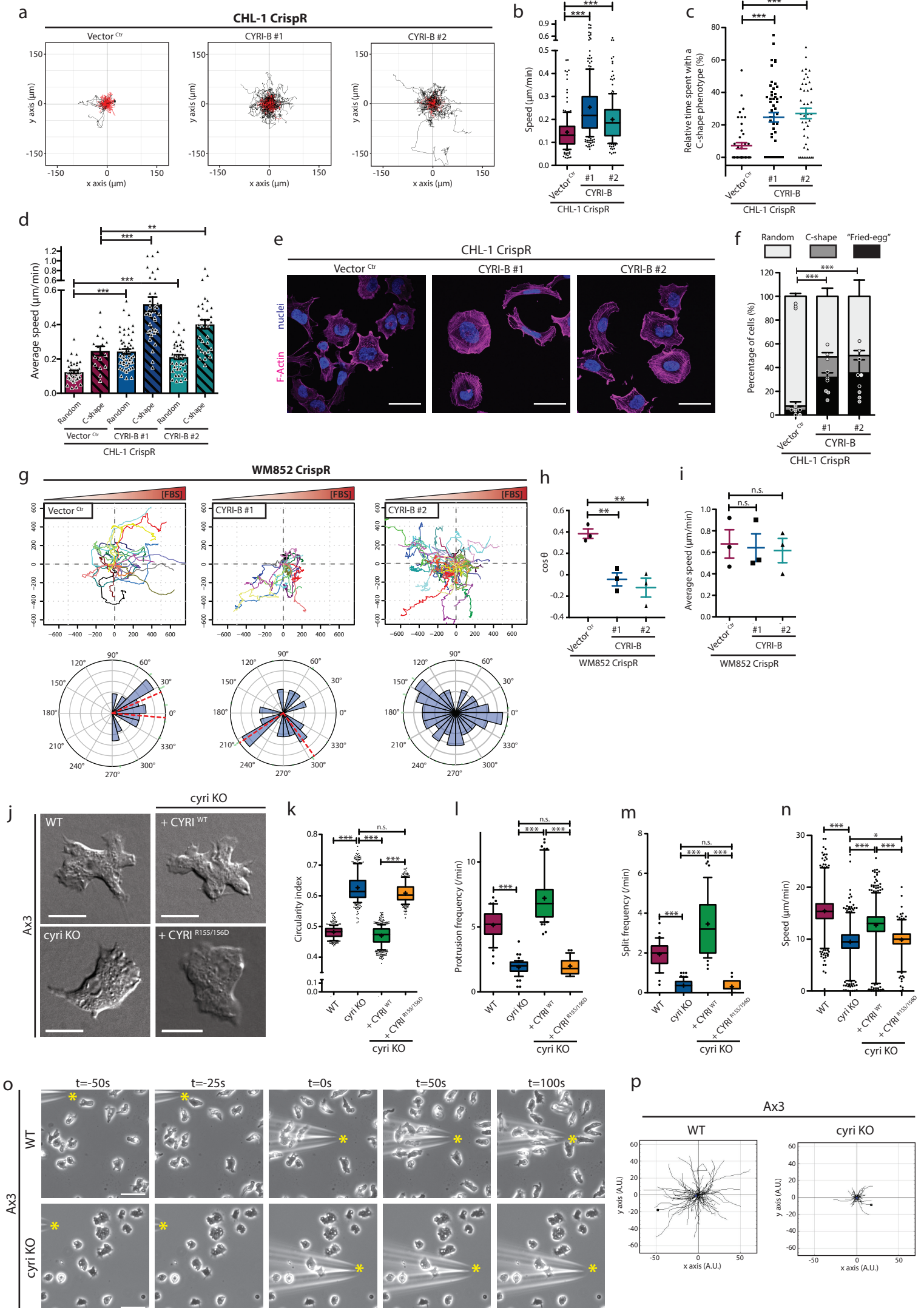
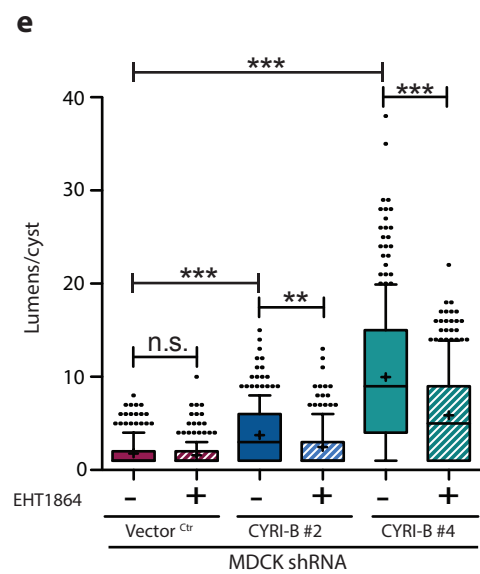
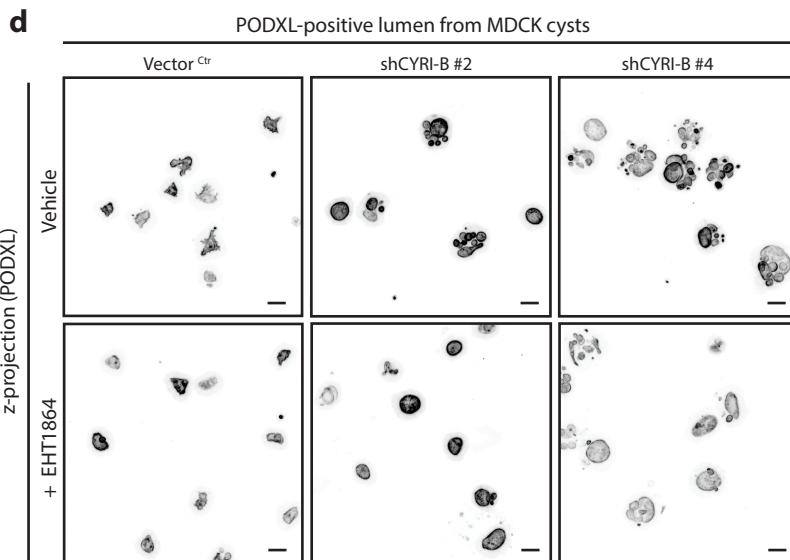
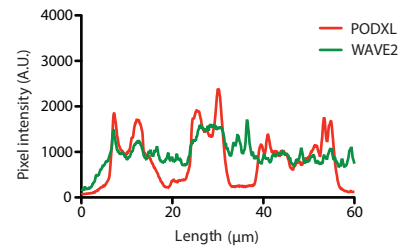
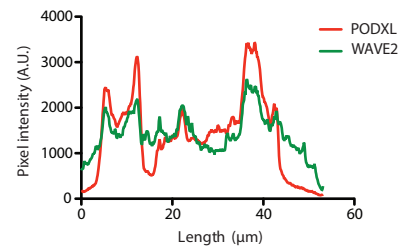
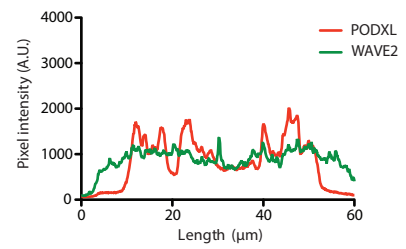
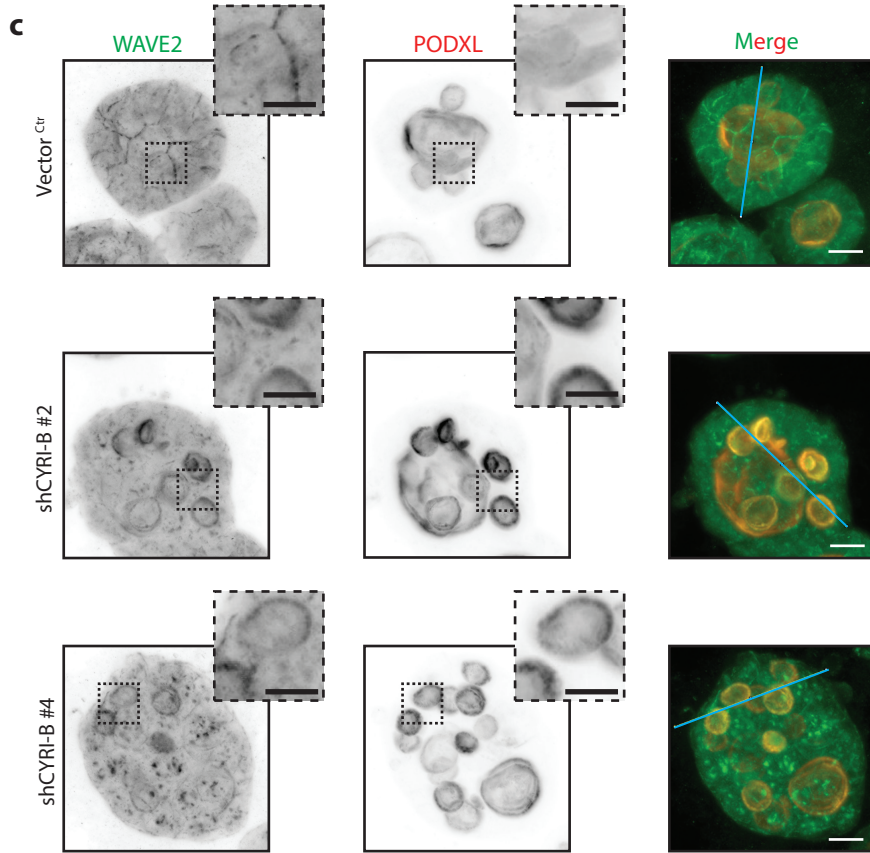
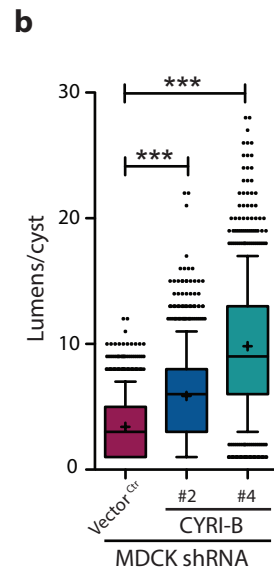
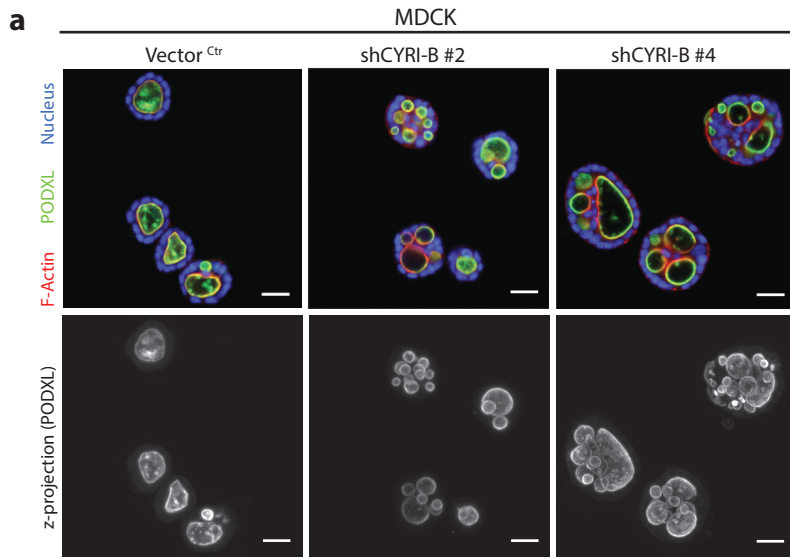
Figure 6

Figure 7



1 **Methods**

2 **Antibodies and constructs**

3 Antibodies and DNA constructs are listed in Supplementary Tables 3 and 4
4 respectively.
5

6 **Alignment and phylogenetic tree**

7 Protein sequences were obtained from Uniprot <http://www.uniprot.org/> and
8 aligned using MacVector software. The phylogenetic tree was constructed based on
9 the major eukaryotic superclasses as previously defined¹⁴ and based on previous
10 identification of Arp2/3 complex and Scar/WAVE complex sequences^{15, 54}. BLAST
11 homology search on the NCBI website <https://blast.ncbi.nlm.nih.gov/Blast.cgi>.
12 *Dictyostelium*, human or a close relative were searched against the complete
13 translated genome of open reading frames from these organisms.
14 HMM logo was generated by feeding the Pfam database of the DUF1394 domain into
15 Skylign⁵⁵.
16

17 **CYRI-B structure prediction**

18 The predicted protein structure of CYRI-B₃₁₋₂₉₂ was generated by the protein
19 homology/analogy recognition engine (Phyre)⁵⁶ using the cytoplasmic fmr1-
20 interacting protein 1 (PDB 3P8C) as a template with 100% homology confidence and
21 18% sequence identity.
22

23 **Mammalian cell lines and growth conditions**

24 CHL-1, HEK293T, COS-7 cells were maintained in Dulbecco's Modified Eagle's
25 Medium supplemented with 10% FBS and 2 mM L-Glutamine (DMEM).

26 ROSA26:CreER^{t2+}; *Ink4*^{-/-};*Cyri-B*^{wt/wt}; *Rac1*^{fl/fl} mouse tail skin fibroblasts and
27 ROSA26:CreER^{t2+};*Ink4*^{-/-}; *Cyri-B*^{fl/fl} mouse embryonic fibroblasts were maintained in
28 DMEM complemented with 1 mg/mL of primocin.

29 COS-7 cells transfected with the doxycycline-inducible system were grown in 10%
30 tetracyclin-free FBS (ClonTech) and treated with 5 µg/mL doxycycline for 48h.

31 MDCK cells were maintained in 5% FBS and 2 mM L-Glutamine supplemented
32 minimum essential medium, high glucose, high sodium bicarbonate.

33 WM852 cells were grown in RPMI supplemented with 10% FBS and 2 mM L-
34 Glutamine.
35

36 All mammalian cell lines used in this study were maintained in 10 cm plastic dishes
37 at 37 °C and 5% CO₂.

38 Cell lines were regularly tested for mycoplasma contamination (MycoAlert - Lonza).
39

40 **CLICK Chemistry of Mammalian CYRI-B**

41 HEK293T cells plated on 24-well plate were transfected with 1 µg of pEGFPN1 or
42 CYRI-B-EGFP (wild-type or G2A mutant) using Lipofectamine 2000 and were
43 processed the next day. C14:0-azide was synthesised as previously described⁵⁷.
44 Transfected HEK293T cells were incubated with 100 µM of C14:0-azide (in DMEM
45 with 1 mg/mL defatted BSA) for 4 h at 37 °C. Cells were washed twice in PBS and
46 lysed on ice for 10 min in 100 µL lysis buffer (150 mM NaCl, 1 % Triton X-100, 50

47 mM Tris-HCl, pH 8.0, containing protease inhibitors). Cell lysates were centrifuged
48 at 10000 x g for 10 min at 4 °C to remove cell debris. Alkyne IR-800 Dye to C14:0
49 azide was conjugated for 1 h at room temperature (RT) with end-over-end rotation
50 by adding an equal volume of freshly mixed click chemistry reaction mixture (10 μM
51 800 CW alkyne infrared dye, 4 mM CuSO₄, 400 μM Tris[(1-benzyl-1H-1,2,3-triazol-
52 4-yl)methyl]amine, and 8 mM ascorbic acid in dH₂O) to the supernatants. GFP-
53 tagged proteins were isolated using the μMACS GFP isolation kit following
54 manufacturer's protocol and resolved by SDS-PAGE as described below. Protein
55 acylation was quantified by expressing the intensity of the CLICK signal relative to
56 the protein signal.

57

58 **Yeast Two-Hybrid screen**

59 Screening was performed at Hybrigenics services *as per* their standard protocols.
60 Briefly, the coding sequence for the constitutively active full-length Rac1
61 (NM_006908.4 ; mutations G12V, C189S) was PCR-amplified and cloned into pB27
62 as a C-terminal fusion to LexA (LexA-Rac1). All libraries use the prey vector pP6.
63 pB27 and pP6 are derived from the original pBTM116⁵⁸ and pGADGH⁵⁹ plasmids,
64 respectively.

65 The bait was screened against the different libraries using a mating approach with
66 YHGX13 (Y187 ade2-101::loxP-kanMX-loxP, mat alpha) and L40deltaGal4 (mat-a)
67 yeast strains as previously described⁶⁰. Positive colonies were selected on a medium
68 lacking tryptophan, leucine and histidine, and supplemented with 3-aminotriazole.
69 The prey fragments of the positive clones were amplified by PCR and sequenced at
70 their 5' and 3' junctions. Interacting proteins were identified in the GenBank
71 database (NCBI).

72

73 **GST Pull-down of Mammalian CYRI-B and GTPases**

74 DH5alpha *E. coli* cells were grown at OD_{600nm} 0.4 and induced for 4h with 0.2 mM
75 IPTG. Pellet was resuspended in ice-cold buffer A (50 mM NaCl, 50 mM Tris-HCl pH
76 7.5, 5 mM MgCl₂, 3 mM DTT) and sonicated, followed by a 30 min spin at 20000 rpm
77 to yield lysate. GST tagged proteins were immobilized on pre-washed glutathione-
78 sepharose beads for 30 min at 4°C with gentle agitation and unbound proteins were
79 washed out 3 times in buffer A.

80 Cells transfected with GFP constructs were collected in ice-cold lysis buffer (100 mM
81 NaCl, 25 mM Tris-HCl pH 7.5, 5 mM MgCl₂, 1X protease and phosphatase inhibitors,
82 0.5% NP-40). 1.5-2 mg of proteins were mixed with pre-equilibrated beads with
83 gentle agitation during 2h at 4°C. Beads were then washed 3 times in washing buffer
84 (100 mM NaCl, 25 mM Tris-HCl pH 7.5, 5 mM MgCl₂), resuspended in sample buffer
85 containing DTT and resolved by SDS-PAGE as described below.

86

87 **MBP Pull-down**

88 Recombinant proteins were purified as mentioned above and immobilized on MBP-
89 trap beads. Beads were mixed with similar amount of recombinant GST-tagged
90 proteins in ice-cold buffer A (see above) containing 0.05% Triton X100. Binding was
91 allowed for 2h at 4°C and beads were then thoroughly washed in ice-cold buffer A.
92 Proteins were eluted by adding boiling sample buffer directly to the beads and

93 prepared for SDS-PAGE.

94

95 **Mutagenesis of Mammalian CYRI-B**

96 Point mutation was inserted using the Q5-site directed kit (New England Biolabs)
97 and following the manufacturer's instructions. Primers were designed using
98 NEBaseChanger - see Supplementary Table 5.

99

100 **Protein purification for SPR analysis**

101 *E. Coli* BL21 CodonPlus (DE3)-RIL (Agilent Tech.) and *E. Coli* BL21 (DE3) pLysS
102 (Promega) were used for GST-tagged and His-Tagged proteins respectively.

103 Pre-culture was grown overnight in L-Broth (LB) containing appropriate antibiotics.
104 Once reaching OD_{600nm} 0.4, protein expression was induced using 0.2 mM IPTG and
105 culture was kept overnight at 20°C under agitation (200 rpm). Cells were lysed in
106 Buffer 1 (200 mM NaCl, 30 mM Tris-HCl pH 7.5, 5 mM MgCl₂, 3 mM β-
107 mercaptoethanol) containing protease inhibitors and passed through a 20,000 psi-
108 pressurised microfluidizer. The soluble fraction was collected by centrifugation (30
109 min, 20000 rpm) and loaded onto an equilibrated GStrap HP or HisTrap HP column
110 using an AKTA machine (GE Healthcare). Proteins were either directly eluted using
111 Buffer 1 containing either 20 mM GSH for GST-tagged proteins or 300 mM Imidazole
112 pH 7.5 for His-tagged proteins. Cleavage on the column was performed overnight
113 with the appropriate protease, flowing at 0.1 ml/min in a loop connected to the
114 AKTA machine. Proteins were gel purified (HiLoad 16/600 Superdrex 75pg or
115 HiLoad 16/600 Superdrex 200pg) in Buffer 2 (150 mM NaCl, 25 mM Tris-HCl pH 7.5,
116 5 mM MgCl₂, 2 mM β-mercaptoethanol), snap-frozen and stored at -80°C.

117

118 **Surface Plasmon Resonance (SPR) protein binding assay**

119 SPR analysis was performed using Biacore T200 (GE Healthcare) equilibrated with
120 buffer 2 (see above) supplemented with 0.5% of surfactant P20. GST-tagged
121 proteins were immobilised at 22°C onto CM5 sensor chip functionalized with anti-
122 GST and reached ~320 RU. Same procedure was used for His-tagged protein onto
123 NTA sensor chip and reached 650 RU. All immobilisation steps were done at a flow
124 rate of 10 μL/min. Serial dilution of each analyte was injected across a reference
125 flow cell and the flow cell containing the ligand at a flow rate of 30 μL/min. Data
126 were solvent corrected, reference subtracted, quality controlled and evaluated using
127 the Biacore T200 evaluation software. Affinity was determined by curve fitting a 1:1
128 binding model.

129

130 **Proximity ligation assay**

131 COS-7 cells expressing CYRI-B-HA and MYC-Rac1 constructs were plated on laminin-
132 coated coverslips and used for DuoLink *in situ* proximity ligation assay (Sigma -
133 mouse and rabbit - Red detection) using the manufacturer's protocol. Mouse anti-HA
134 (Covance) and Rabbit anti-MYC-tag (CST) were used at 1:400 and 1:200 respectively.
135 Incubation with either antibody was performed as a negative control.

136

137 **Enforced mitochondrial localisation**

138 The Rac1A cDNA (gift of A. Kortholt, University of Groningen) was mutagenised to

139 P29S/Q61L the stop codon removed. It was cloned N-terminal to mCherry-
140 mitochondrial anchor, or N-terminal to mCherry to give a cytosolic version.
141 Likewise, PakB-CRIB was cloned N-terminal to either GFP alone (to give a soluble
142 CRIB fusion) or GFP-mito (to give a mitochondrial-targeted version). CYRI was
143 similarly used in its WT or R155D R156D double mutant. The mitochondrial anchor
144 consists of the C-terminal tail (aa 602-658) of *gemA*, the *Dictyostelium*
145 mitochondrial-anchored Rho1/2 GTPases.

146 Live cell images were acquired at separate times using single-channel hardware
147 setups to ensure zero channel bleed-through or dual excitation of fluorophores. To
148 note, the cells move between image captures. Dual images were captured using a
149 double band-pass filter that allows both red and green signals to pass
150 simultaneously. The same cells are shown in the red, green and dual images.

151
152

153 **Transfection, siRNA Treatment and Knockout Mammalian Cells.**

154 Oligos used are listed in Supplementary Table 5.

155 Cells were plated a day before transfection at 70% of confluence and later
156 transfected using Lipofectamine 2000 according to the manufacturer's instructions.
157 2-5 µg of DNA was used per reaction based on a 6-well plate format.

158 siRNA oligonucleotides targeting CYRI-B (Qiagen): Mouse tail fibroblasts and COS-7
159 cells were respectively treated with 75 nM of *Mus musculus* CYRI-B siRNA and 25
160 nM of *Homo sapiens* CYRI-B siRNA (recognised *Cercopithecus aethiops*) or matched
161 concentration of control siRNA (AllStars Negative siRNA – Qiagen) were transfected
162 using Lullaby transfection reagent according to manufacturer's instructions. The
163 same step was repeated 48h later and cells were analysed after 24h.

164 For CrispR/Cas9 mediated knock out, sgRNA were selected using the MIT CrispR
165 designing tool (<http://crispr.mit.edu/>). Annealed oligonucleotides were cloned into
166 pLentiCrispRv2-Puro. Briefly, HEK293T cells were seeded at 1.5×10^6 cells/10cm
167 dish. Cells were transfected with 10 µg of the selected plasmid (Vector^{Ctrl} or
168 containing a gRNA against CYRI-B) 7.5 µg of pSPAX2 (Addgene 8454) and 4 µg of
169 pVSVG (Addgene 12260) in a final volume of 440 µL of sterile water, and
170 complemented with 500 µL 2X HBS and 120 mM CaCl₂. Solution was incubated 30
171 min at 37°C before adding to HEK293T cells. Medium was removed after 24h and
172 replaced by 6 mL of 20 % FBS DMEM. Meanwhile, recipient cells were plated at $1 \times$
173 10^6 cells/10cm dish. The day after, supernatants were filtered through a 0.45 µm
174 pore membrane and mixed with 25 µg of hexadimethrine bromide (4.2 µg/mL final)
175 before infecting recipient cells. Infection was repeated the next day and stably
176 transfected cells were selected with 1 µg/mL of puromycin.

177

178 Same procedure was used for lentiviral infection of the MDCK cells and cells were
179 selected with 5 µg/mL of puromycin.

180

181 For CrispR COS-7 *cyri-b* knockout cells, human gRNAs against *CYRI-B* (CrispR#1 or
182 #2 - See Table 5) were cloned into a pSpCas9(BB)-2A-GFP vector (Addgene
183 plasmid #48138) using the restriction enzyme *BbsI* as described in⁶¹ COS-7 cells
184 were seeded onto 6 cm dishes and transfected the day after using Lipofectamine

185 2000 with 5 µg of pSpCas9(BB)-2A-GFP (empty vector or *CYRI-B* targeting CrispR
186 gRNA) following the manufacturers guidelines. Cells were grown for approximately
187 24 h before FACS sorting. The transfected cells were trypsinised, resuspended in
188 serum free DMEM with DAPI (1 µg/ml) and filtered through a 0.45 µm pore
189 membrane for FACS. For FACS, gates were drawn to sort by cell size, live/dead and
190 GFP positive cells. GFP positive sorted cells were incubated with DMEM complete
191 and left to grow at normal culturing conditions. Knockouts for *CYRI-B* were analysed
192 by western blotting.

193

194 Generation of knockout mouse embryonic fibroblast and mouse tail skin fibroblast
195 cell lines were obtained by adding 1 µM of hydroxytamoxifen in the growth medium
196 every 3 days over 7 days.

197

198

199 **FRET imaging of Mammalian Cells**

200 The Rac1-Raichu-mTq2-sREACH probe is described in²⁹. Cells were transfected with
201 the probe, plated the day after on laminin and imaged. FRET images were acquired
202 with the Nikon FLIM/TIRFsystem Z6014 microscope equipped with a Plan
203 Apochromat 63x/1.45 oil objective and a 465 nm LED. Dishes were placed in a 37°C
204 heated chamber perfused with 5% CO₂. FRET efficiency was calculated by
205 standardizing the probe lifetime to the average lifetime of the donor alone as
206 follows:

$$FRET\ efficiency\ (\%) = \frac{Average\ lifetime\ donor - Lifetime\ probe}{Average\ lifetime\ donor} \times 100$$

207

208 **Active Rac1 pulldown**

209 COS-7 cells were plated on laminin-coated dishes for 1h, washed twice with ice-cold
210 PBS and lysed using 50 mM Tris-HCl pH 7.4, 500 mM NaCl, 1% Triton X-100, 0.5%
211 sodium deoxycholate, 10 mM MgCl₂, 1X protease and phosphatase inhibitors.
212 Cleared lysates were incubated with recombinant GST or GST-CRIB-PBD obtained
213 from DH5alpha cells as described above. 1-1.5 mg of lysate were incubated for 2 h at
214 4°C with a similar amount of GST-construct immobilised on glutathion-sepharose
215 beads. Beads were washed 3 times with 50 mM Tris-HCl pH 7.4, 500 mM NaCl, 10
216 mM MgCl₂ and prepared for SDS-PAGE analysis as described below.

217

218 **SDS-PAGE and Western Blotting of Mammalian Cells**

219 Lysates were collected on ice by scraping cells in RIPA Buffer (150 mM NaCl, 10 mM
220 Tris-HCl pH 7.5, 1 mM EDTA, 1% Triton X100, 0.1% SDS, 1X protease and
221 phosphatase inhibitors) and centrifuged 10 min at 15000 rpm and 4°C. Protein
222 concentration was measured at OD_{600nm} using Precision Red.

223 20-40 µg of protein were resolved on a NuPAGE Novex 4-12% Bis-Tris gels and
224 transferred onto a nitrocellulose membrane using the BioRad system. Membranes
225 were blocked in 5% non-fat milk in TBS-T (10 mM Tris pH 8.0, 150 mM NaCl, 0.5%
226 Tween 20) during 30 min before overnight incubation with primary antibodies at
227 4°C. Membranes were washed 3x 5 min in TBS-T and incubated 1h with Alexa-Fluor

228 conjugated secondary antibodies. Blots were then washed 3x 5 min and imaged
229 using the LiCor Odyssey CLx.
230 All images were then analysed using Image StudioLite v.5.2.5.

231

232 **Immunofluorescence of Mammalian Cells**

233 Cells were collected and plated onto sterile 13mm glass coverslips coated overnight
234 at 4°C with 10 µg/mL of rat-tail collagen I, 10 µg/mL fibronectin or 10 µg/mL
235 laminin diluted in PBS. Coverslip were washed 3x in PBS before seeding cells. Cells
236 were fixed with 4% paraformaldehyde for 10 min, permeabilised (20 mM Glycine,
237 0.05% Triton X100) for 10 min and blocked with 5% BSA-PBS for 30 min. Primary
238 and secondary antibodies were diluted in blocking buffer and incubated 1h in a dark
239 and humidified chamber. Coverslips were washed twice in PBS and once in water
240 before being mounted on glass slides using ProLong Gold antifade reagent. Images
241 were taken using an inverted Olympus FV1000 confocal microscope using a Plan
242 Apochromat N 63x/1.40 oil SC or an Uplan FL N 40x/1.30 oil objective.
243 Images were processed and analysed using Fiji software (ImageJ v1.48t)¹⁶.

244

245 **Membrane dynamics analysis**

246 CHL-1 cells were transfected with GFP-LifeAct (5 µg AMAXA kit-T, program T-020)
247 and incubated overnight in complete DMEM. Cells were then plated onto a glass
248 bottom dish coated with laminin for 3 h before imaging within a contained unit at
249 37°C and 5% CO₂. Time-lapse images were taken using a Nikon microscope with a
250 CoolLED GFP filter set (470 nm LED) and a Nikon Plan Apo VC 100x/1.4 NA oil
251 immersion objective and captured using a Photometrics PRIME camera. GFP images
252 were taken at 1 frame per second for a total of 3 min. For each frame, a binary mask
253 was made of the cell based on the intensity of its LifeAct signal, and the intensity of
254 an associated edge image made by Canny edge detection. Differences between binary
255 images from one frame to the next were used to find areas of extension or retraction,
256 with extended areas positively valued and retracted areas negatively valued. Co-
257 ordinates for an outline of the binary image of each frame were extracted from the
258 ROI class in ImageJ, and were used to measure the mean intensity of the
259 corresponding difference image in a 5x5 px area. These values were then written for
260 each cell to a new 2D image that we refer to as an "unwrapped kymograph", with
261 each two rows representing one frame and each column representing one outline
262 coordinate point for that frame. After smoothing this unwrapped kymograph, areas
263 of protrusion were identified by thresholding, with their extension in the y direction
264 (time) measured. This gave us an estimate of the active lifetime of each protrusion,
265 and a mean protrusion lifetime for each cell. Images were processed using
266 Metamorph and Fiji softwares.

267 Plugin used for creating kymograph will be provided upon reasonable request.

268

269 **Rac1 photo activation**

270 *Transfection protocol:* MEFs were transiently transfected by electroporation (Amaya
271 kit T) with 5 µg of photoactivatable Rac1 plasmid³¹ (pTriEx-LOV2-Ja-Rac1-mCherry).
272 The transfected cells were suspended in complete DMEM media, and plated onto
273 laminin-coated glass-bottom 35 mm dishes. After several hours, the media was

274 replaced with serum-free DMEM and incubated overnight in darkness.
275 *Imaging:* Imaging was performed on a Zeiss 880 confocal microscope with a stage
276 incubator perfused with CO₂. Time-lapse imaging of moderate mCherry expressing
277 cells was done for 150 frames at 2 second intervals between frames. Two images
278 were collected for each frame at 568 nm with bi-directional scanning averaged over
279 two frames to image the mCherry tag, and a transmitted light detector to show a
280 bright field image of the cell morphology, both at 1024x1024 resolution. An initial
281 29 frames (1 minute) was collected with 568 nm excitation to document baseline
282 protrusive activity. Photoactivation of Rac1 was started at frame 30, and continued
283 for each frame to 150, with a pulse of 458 nm excitation in a 100 pixel diameter
284 region of interest. The 568 nm excitation was at 7.5% laser power, with gain of 600-
285 800 depending on the brightness of the cell, and the pinhole set at 300 to maximize
286 collection of light levels and depth of field to capture ruffles. The 458 nm excitation
287 used laser power of 10% and scan speed set for a pixel dwell time of 8 μsec.
288 Movies were processed using the Plugin found in Supplementary Note 1
289

290 **Chemotaxis assay**

291 Chemotaxis assays with WM852 human melanoma cells were performed as
292 described in³⁵. Briefly 8 x 10⁴ cells were seeded onto fibronectin coated coverslips
293 and left overnight in serum-free RPMI. Coverslips were mounted onto Insall
294 chambers with RPMI containing 10% fetal bovine serum as the chemoattractant,
295 and images were taken every 15 min for 48 h with a Nikon TE2000-E time-lapse
296 microscope using Metamorph software. Cells were manually tracked using MTrackJ
297 plugin in Fiji. All cells that moved independently of other cells were chosen for
298 tracking. Approximately 120 cells were tracked for each condition from 3
299 independent repeats per condition (see also legend Figure 6).
300

301 **Random Migration Assay for Mammalian Cells**

302 6-well glass bottom plates were coated overnight as described above. 1x10⁵ cells
303 were plated and imaged every 10 min for 17 h using a Nikon TE2000 microscope,
304 PlanFluor 10x/0.30 objective and equipped with a heated CO₂ chamber. Images were
305 analysed using Fiji software⁶³ (ImageJ v1.48t). Individual cells were tracked using
306 the mTrackJ plugin, and spider plots were generated using the chemotaxis and
307 migration tool plugin (v.1.01).
308

309 ***Dictyostelium discoideum* Cells**

310 Axenic *D. discoideum* strains Ax3 was used as wildtype. *cyri* knockout cells were
311 generated in Ax3 genetic backgrounds. Ax3-derived *napA* KO cells are described
312 previously⁶⁴. Cells were grown in HL5 medium (Formedium) with 100 U/ml
313 penicillin and 100 μg/ml streptomycin in 10 cm plastic Petri dishes and incubated at
314 21°C.
315

316 ***Dictyostelium discoideum* GFP-Trap with Formaldehyde Crosslinking**

317 Cells were collected in PBS and lysed by adding ice-cold 3x lysis/crosslinking buffer
318 (1x buffer: 20 mM HEPES pH 7.4, 2 mM MgCl₂, 3% formaldehyde, 0.2% Triton X-
319 100). After 5 min with gentle agitation at 4 °C, formaldehyde was quenched for

320 10min on ice using 1.75 M Tris pH 8.0. Samples were centrifuged at 22000g for 4
321 min at 4 °C. Pellet was successively washed and resuspended with 1 mL of ice cold
322 quenching buffer (0.4 M Tris pH 8.0, 0.2% Triton X-100), wash buffer A (100 mM
323 HEPES pH 7.4, 2 mM MgCl₂, 0.2% Triton X-100) and wash buffer B (100 mM HEPES
324 pH 7.4, 2 mM MgCl₂), with 3 min centrifugation step between washes. Final
325 resuspension was performed using 1mL of ice-cold RIPA buffer (50 mM Tris-HCl pH
326 8.0, 150 mM NaCl, 0.5% Triton X-100, 0.5% sodium deoxycholate, 0.15% SDS, 5 mM
327 EDTA, 2 mM DTT) and incubated 1h at 4 °C with gentle agitation. Supernatants were
328 mixed with pre-equilibrated GFP-Trap beads (Chromotek) following manufacturer's
329 protocol. Beads were washed 3x with 50 mM Tris-HCl pH 8.0, 150 mM NaCl, 5 mM
330 EDTA followed by 1 wash with 10 mM Tris-HCl pH 8.0. Samples were eluted after
331 incubation with 2x SDS loading buffer and heating 10 min at 70°C before loading on
332 a SDS-PAGE.

333

334 *Dictyostelium discoideum* GFP-NAP1 'in gel' Proteolytic Digestion - Mass 335 Spectrometry Analysis

336 Eluates from GFP-NAP1 immunoprecipitation were separated by SDS-PAGE and
337 stained with Coomassie blue. Each gel lane was divided in 6 slices and digested⁶⁵.
338 Tryptic peptides from in gel digestions were separated by nanoscale C₁₈ reverse-
339 phase liquid chromatography using an EASY-nLC II (Thermo Fisher Scientific)
340 coupled online to a Linear Trap Quadrupole - Orbitrap Velos mass spectrometer
341 (Thermo Scientific) and desalted using a pre-column C18 NS-MP-10 100µm i.d. x 0.2
342 cm of length (NanoSeparations). Elution was at a flow of 300 nl/min over a 90 min
343 gradient, into an analytical column C18 NS-AC-11 75µm i.d. x 15 cm of length
344 (NanoSeparations). For the full scan a resolution of 30,000 at 400 Th was used. The
345 top ten most intense ions were selected for fragmentation in the linear ion trap
346 using Collision Induced Dissociation using a maximum injection time of 25 ms or a
347 target value of 5000 ions. MS data were acquired using the XCalibur software
348 (Thermo Fisher Scientific).

349

350 Raw data obtained were processed with MaxQuant version 1.5.5.1⁶⁶ and Andromeda
351 peak list files (.apl) generated were converted to Mascot generic files (.mgf) using
352 APL to MGF Converter [[http://www.wehi.edu.au/people/andrew-webb/1298/apl-
353 mgf-converter](http://www.wehi.edu.au/people/andrew-webb/1298/apl-mgf-converter)]. Generated MGF files were searched using Mascot (Matrix Science,
354 version 2.4.1), querying dictyBase⁶⁷ (12,764 entries) plus an in-house database
355 containing common proteomic contaminants and the sequence of GFP-NAP1. The
356 common contaminant and reverse hits (as defined in MaxQuant output) were
357 removed.

358 Mascot was searched assuming trypsin digestion allowing for two miscleavages with
359 a fragment ion mass tolerance of 0.6 Da and a parent ion tolerance of 15 ppm. The
360 iodoacetamide derivative of cysteine was specified in Mascot as a fixed modification,
361 and oxidation of methionine and phosphorylation of serine, threonine and tyrosine
362 were specified in Mascot as variable modifications. Scaffold (version 4.3.2,
363 Proteome Software) was used to validate MS/MS based peptide and protein
364 identifications. Peptide identifications were accepted if they could be established at
365 greater than 95.0% probability as specified by the Peptide Prophet algorithm,

366 resulting in a peptide false discovery rate (FDR) of 0.63%²⁰. For label-free
367 quantification, proteins were quantified according to the label-free quantification
368 algorithm available in MaxQuant⁶⁸.

369 Significantly enriched proteins were selected using a Welch-test analysis with a 5%
370 FDR.

371 The mass spectrometry proteomics data have been deposited to the
372 ProteomeXchange Consortium via the PRIDE partner repository with the dataset
373 identifier PXD010460.

374

375 **Generation and Validation of *cyri*-knockout and rescued *Dictyostelium*** 376 ***discoideum***

377 Primers used are detailed in Supplementary Table 5.

378 Standard methods were used for construction of all *Dictyostelium* knockout and re-
379 expression vectors⁶⁹. A linear CYRI knockout construct (2758 bp in length), which
380 consisted of a blasticidin resistance (Bsr) cassette flanked by sequences matching 5'
381 and 3' regions in the *CYRI* (DDB_G0272190 identifier at dictybase.org) gene locus
382 (18pb cross-over), was made by PCR amplification using the primers set 1 (5' arm)
383 and set 2 (3' arm). PCR-amplified arms were combined with the Bsr cassette in a
384 using the primers set 3.

385 Knockout clones were screened/validated by PCR, with primers set 4. *cyri*-knockout
386 yield a 2450 bp PCR product, random integrants (clones with a KO construct
387 integration elsewhere in the genome) and wild-type yield a 1983 bp PCR product.

388

389 Vector for expression of untagged CYRI was obtained by sub-cloning CYRI's
390 genomic coding region into pDM358⁶⁹. A REMI³⁷ (non extra-chromosomal) vector
391 was derived from this by removal of the *Dictyostelium* plasmid propagation genes
392 and re-ligation of the vector backbone. This construct, while still having a strong
393 promoter, is expected to be present in just one copy per cell.

394

395 **Transformation of *Dictyostelium discoideum***

396 3.0×10^7 cells/transformation were first centrifuged (3 min, 330 x *g*, 4°C), washed
397 with 10 ml ice-cold electroporation buffer (E-buffer; 10 mM sodium phosphate
398 buffer pH 6.1, 50 mM sucrose), and resuspended in 400 µl ice-cold E-buffer. Cells
399 were transferred into an ice-cold 0.2 cm electroporation cuvette and incubated 5
400 min with 0.5-1.0 µg of DNA on ice. Cells were electroporated (BTX-Harvard
401 Apparatus ECM 399) at 500V, giving a time constant of 3-4ms. Cells were
402 immediately transferred to HL5 medium in Petri dishes. Appropriate selection (50
403 µg/ml hygromycin or 10 µg/ml G418) was added the next day. For REMI
404 transfections, 10 µg of linearized DNA and 50 U of restriction enzyme were used, in
405 0.4cm cuvettes with a Bio-Rad Gene Pulser II set at 1.2kV and 3µF.

406

407 ***Dictyostelium discoideum* CYRI inclusion body purification**

408 BL21(DE3) pLysS cells were grown to OD_{600nm} 0.2 and induced with 0.2 mM IPTG for
409 4h. Cells were pelleted, frozen and resuspended with 80 mL of lysis buffer (50 mM
410 Tris-HCl pH 8.0, 25 % sucrose (w/v), 1 mM EDTA) per 100g of cells. Cells were lysed
411 by adding 1% lysozyme (w/v) and kept on ice for 30 min. Lysate was resuspended

412 with 10 mM MgCl₂, 1mM MnCl₂, 10µg/mL DNase I and kept for another 30 min on
413 ice. Finally, 200 mL of detergent buffer (0.2 M NaCl, 1% deoxycholic acid (w/v), 1%
414 NP40, 20 mM Tris-HCl pH 7.5, 2 mM EDTA) was added to the lysate, which is then
415 centrifuged at 5000 x g for 10 min. Pellet is then washed in 0.5% NP40, 1 mM EDTA
416 and this step is repeated until a tight white pellet is obtained.

417

418 ***Dictyostelium discoideum* CYRI antibody production**

419 Inclusion bodies were dissolved in sample buffer with DTT and loaded onto a 10%
420 Bis-Tris acrylamide gel at 70V at 4 °C. Gel was Coomassie stained and fragments of
421 the band corresponding to CYRI was sent to BioGenes for injection into 2 rabbits.
422 Bleeds were collected every second week after initial immunisation/boost and
423 tested by western blot.

424 (Terminal bleed from rabbit 27724 after 5th boost used at 1:100).

425

426 ***Dictyostelium discoideum* Under-agarose Chemotaxis Assay**

427 This assay is based on a previous study⁷⁰. Surface of the 30 mm glass bottom dish
428 (MatTek) was coated with 10 mg/ml BSA for 10 min, washed with dH₂O and dried
429 for 5 min inside a laminar flow cabinet. 0.4% w/v SeaKem GTG agarose in SIH
430 medium (Formedium) containing 10 µM folate was poured and set for 1h. A well was
431 cut in the agarose and 2x10⁶ cells/mL placed in it. After 3-4h cells were imaged by
432 Phase contrast and DIC microscopy with a Nikon Eclipse TE2000-E microscope
433 system equipped with a QImaging RETIGA EXi FAST 1394 CCD camera and a pE-100
434 LED illumination system (CoolLED) at 525 nm. A 10×/ 0.45 NA Ph1 objective and a
435 60×/1.40 NA apochromatic DIC objective were used for phase contrast and DIC,
436 respectively. Imaging was controlled through the µManager 1.4.9 software. All
437 microscopy was carried out at RT and images were analysed with ImageJ/Fiji 1.49i.
438 Pseudopod rate and split frequency was analysed from the DIC movies and manually
439 quantified frame by frame. For analysis of cell circularity, speed and migration
440 parameters, automated tracking plugins were developed for ImageJ (see Plugin2 in
441 Supplementary note 2). More information will be supplied upon reasonable request.

442

443 ***Dictyostelium discoideum* development assay**

444 Cells were harvested from axenic growth plates, washed twice in phosphate buffer
445 (10 mM Na/K phosphate pH 6.5) containing 2 mM MgCl₂ and 1mM CaCl₂, and plated
446 on 1% w/v agar prepared in the same buffer. For time-lapse imaging we used a
447 Nikon Eclipse TE2000-E microscope fitted with a Prior ProScan II moving stage, and
448 equipped with a QImaging RETIGA EXi FAST 1394 CCD camera and a pE-100 LED
449 illumination system (CoolLED) at 525 nm.

450

451 **cAMP needle assay**

452 Cells were developed as described above until territories began to form, indicating
453 production and responsiveness to cAMP waves. Cells were harvested and placed into
454 phosphate buffer and their response to 10 µM cAMP (Eppendorf Injectman NI2
455 microinjector with Femtotips II) was monitored by timelapse microscopy (1
456 frame/5sec) using a Zeiss Axiovert A1 body with a plan/neofluar 20x 0.5NA
457 objective combined with a QI RETiga camera.

458

459 **HSPC300-GFP analysis**

460 Wild type or *cyri* KO Ax3 cells were transfected with HSPC300-GFP as described
461 above and timelapse movies were obtained using a Zeiss 880 confocal microscope.
462 Processed images were used to obtain the unwrapped kymograph. Plugin used for
463 this analysis will be provided upon reasonable request.

464

465

466 **3D MDCK cysts - Culture**

467 shRNA-expressing MDCK cells were split 1:10 the day before plating in 3D, in
468 puromycin-free medium. Chilled 8-well chamber slides were coated by spreading 5
469 μ L of undiluted Matrigel over the well surface and transferred to 37°C incubator for
470 10 min. MDCK cells were diluted to 4×10^4 cells/mL in puromycin-free medium and
471 thoroughly disaggregated by pipetting. Matrigel was then diluted to 4% in MEM
472 medium and mixed with the similar volume of cells diluted at 1.5×10^4 cells/mL,
473 bringing the final Matrigel concentration to 2%. Wells were filled with 300 μ L of the
474 cell-Matrigel mix and cysts were grown 5 days at 37°C.

475

476 **3D MDCK cysts - Immunofluorescence and Imaging**

477 Medium was aspirated and wells were quickly washed twice with PBS. Cysts were
478 fixed using 4% PFA for 10 min, washed, and permeabilised for 10 min at RT using
479 0.5% Triton X100 diluted in PBS. Cells were blocked for 30 min using PFS (0.7%
480 (w/v) fish skin gelatin in 0.025% Saponin-PBS). Primary antibodies were diluted in
481 PFS and incubated overnight at 4°C with gentle shaking. Cysts were washed 3x in
482 PFS at RT. Secondary antibodies, nuclear dye and Phalloidin were diluted at 1:200 in
483 PFS and incubated for an hour at RT before further washes. Chambers were then
484 kept sealed in 0.02% NaN_3 -PBS at 4°C until analysis. Cysts were imaged using the
485 Nikon A1R Z6005 confocal microscope using either a Plan Apochromat 20x/0.75
486 DIC N2 or a Plan Fluor 10x/0.30 DIC L/N1 objective. In order to sharpen images,
487 factor line averaging was set up at 4. Z-stack images were acquired with a 4 μ m
488 increment step from the bottom to the top of the cyst.

489

490 **Statistics and Reproducibility**

491 Data sets were analysed using Prism5 v5.0c and Prism7. Differences between
492 groups were tested for normality and then analysed using the appropriate statistical
493 test, mentioned in each figure legend. Error bars represent standard error of the
494 mean (S.E.M) unless stated otherwise. Significance levels are given as follows: ns:
495 $p > 0.05$; * $p \leq 0.05$; ** $p \leq 0.01$; *** $p \leq 0.001$. Cochran-Mantel-Haenszel test was
496 generated using R software and p -values are mentioned when appropriate.
497 All experiments were repeated independently as biological repeats at least 3x,
498 unless stated otherwise, and always gave similar trends. Individual values are
499 available in Supplementary Table 6.

500

501 **Data Availability**

502 Mass spectrometry data have been deposited in ProteomeXchange with the primary
503 accession code PXD 010460. Source data for Figs 1-7 and Supplementary Figs 2-6

504 have been provided as Supplementary Table 6. All other data supporting the
505 findings of this study are available from the corresponding authors on reasonable
506 request.

507

508 **Code Availability**

509 The code used for analysis of cell protrusions in Figure 5 is available in
510 Supplementary Note 1. The code used for tracking *Dictyostelium* migration under
511 agarose is available in Supplementary Note 2. Homemade plugins from this study
512 will be made available from the corresponding authors upon reasonable request.

513

514

515 **References**

516

- 517 54. Kollmar, M., Lbik, D. & Enge, S. Evolution of the eukaryotic ARP2/3 activators
518 of the WASP family: WASP, WAVE, WASH, and WHAMM, and the proposed
519 new family members WAWH and WAML. *BMC Res Notes* **5**, 88 (2012).
- 520 55. Wheeler, T.J., Clements, J. & Finn, R.D. Skylign: a tool for creating informative,
521 interactive logos representing sequence alignments and profile hidden
522 Markov models. *BMC Bioinformatics* **15**, 7 (2014).
- 523 56. Kelley, L.A. & Sternberg, M.J. Protein structure prediction on the Web: a case
524 study using the Phyre server. *Nat Protoc* **4**, 363-371 (2009).
- 525 57. Greaves, J. *et al.* Molecular basis of fatty acid selectivity in the zDHHC family
526 of S-acyltransferases revealed by click chemistry. *Proc Natl Acad Sci U S A*
527 **114**, E1365-E1374 (2017).
- 528 58. Vojtek, A.B. & Hollenberg, S.M. Ras-Raf interaction: two-hybrid analysis.
529 *Methods Enzymol* **255**, 331-342 (1995).
- 530 59. Bartel, P., Chien, C.T., Sternglanz, R. & Fields, S. Elimination of false positives
531 that arise in using the two-hybrid system. *Biotechniques* **14**, 920-924 (1993).
- 532 60. Fromont-Racine, M., Rain, J.C. & Legrain, P. Toward a functional analysis of
533 the yeast genome through exhaustive two-hybrid screens. *Nat Genet* **16**, 277-
534 282 (1997).
- 535 61. Ran, F.A. *et al.* Genome engineering using the CRISPR-Cas9 system. *Nat*
536 *Protoc* **8**, 2281-2308 (2013).
- 537 62. Martin, K.J. *et al.* Accepting from the best donor; analysis of long-lifetime
538 donor fluorescent protein pairings to optimise dynamic FLIM-based FRET
539 experiments. *PLoS One* **13**, e0183585 (2018).
- 540 63. Schneider, C.A., Rasband, W.S. & Eliceiri, K.W. NIH Image to ImageJ: 25 years
541 of image analysis. *Nat Methods* **9**, 671-675 (2012).
- 542 64. Ibarra, N., Blagg, S.L., Vazquez, F. & Insall, R.H. Nap1 regulates Dictyostelium
543 cell motility and adhesion through SCAR-dependent and -independent
544 pathways. *Curr Biol* **16**, 717-722 (2006).
- 545 65. McGarry, D.J., Shchepinova, M.M., Lilla, S., Hartley, R.C. & Olson, M.F. A Cell-
546 Permeable Biscyclooctyne As a Novel Probe for the Identification of Protein
547 Sulfenic Acids. *ACS Chem Biol* **11**, 3300-3304 (2016).

- 548 66. Cox, J. & Mann, M. MaxQuant enables high peptide identification rates,
549 individualized p.p.b.-range mass accuracies and proteome-wide protein
550 quantification. *Nat Biotechnol* **26**, 1367-1372 (2008).
- 551 67. Fey, P., Dodson, R.J., Basu, S. & Chisholm, R.L. One stop shop for everything
552 Dictyostelium: dictyBase and the Dicty Stock Center in 2012. *Methods Mol*
553 *Biol* **983**, 59-92 (2013).
- 554 68. Keller, A., Nesvizhskii, A.I., Kolker, E. & Aebersold, R. Empirical statistical
555 model to estimate the accuracy of peptide identifications made by MS/MS
556 and database search. *Anal Chem* **74**, 5383-5392 (2002).
- 557 69. Veltman, D.M., Akar, G., Bosgraaf, L. & Van Haastert, P.J. A new set of small,
558 extrachromosomal expression vectors for Dictyostelium discoideum. *Plasmid*
559 **61**, 110-118 (2009).
- 560
- 561 70. Woznica, D. & Knecht, D.A. Under-agarose chemotaxis of Dictyostelium
562 discoideum. *Methods Mol Biol* **346**, 311-325 (2006).
- 563